New Results on the Simulation of Particulate Flows

M. Uhlmann

Departamento de Combustibles Fósiles, CIEMAT
Avenida Complutense 22, 28040 Madrid, Spain
markus.uhlmann@ciemat.es

March 2004

Abstract

We propose a new immersed boundary method for the simulation of particulate flows. The fluid-solid interaction force is formulated in a direct manner, without resorting to a feed-back mechanism and thereby avoiding the introduction of additional free parameters. The regularized delta function of Peskin (Acta Numerica, 2002) is used to pass variables between Lagrangian and Eulerian representations, providing for a smooth variation of the hydrodynamic forces while particles are in motion relative to the fixed grid. The application of this scheme to several benchmark problems in two space dimensions demonstrates its feasibility and efficiency.

Chapter 1

Introduction

In a previous report [1] several schemes for the simulation of particulate flows by means of a fictitious domain method were compared and later further implemented on parallel machines [2]. It was found that the immersed boundary method as presented in reference [3] was capable of producing satisfactory results in various test cases. However, a drawback of this method is the presence of *ad hoc* parameters which control the stiffness and damping characteristics of virtual forces governing the motion of each element of the fluid-solid interface. Furthermore, the characteristic time scales of these perturbations need to be resolved leading to quite severe restrictions of the time step.

Alternative methods where the additional forces which impose rigid body motion upon the fluid are determined *directly* offer a clear advantage in terms of efficiency. However, they were found to present a different type of serious drawbacks. The implicit method of reference [4] as well as the explicit method presented in [5] both lead to unacceptably strong oscillations in the force term when the solid particle is in motion w.r.t. the fixed grid. This phenomenon is due to insufficient smoothing during the interpolation procedure. The "rigidity" method of reference [6] remedies this problem only partially by using the solid fraction of a grid cell as a weight factor for the force term.

In the present note, we propose a new variant of a direct forcing scheme which borrows heavily from the immersed boundary method. In particular, we use Peskin's regularized delta function [7] for the smooth transfer of quantities between Eulerian and Lagrangian positions. Moreover, the present scheme does not rely upon virtual forces and therefore no additional parameters are introduced. The allowable time step is expected to be of the same order as found in previous direct methods.

Chapter 2

New direct forcing method

2.1 Geometrical definitions

We define a number of n_L marker elements around the circumference of a circular solid object, as shown in figure 2.1. As can be seen, the elements are equi-partitioned sectors of an annulus with inner and outer radii r_1, r_2, respectively. The actual particle radius r_c is located at the midpoint of these two radii:

$$r_c = \frac{r_2 + r_1}{2}\,. \tag{2.1}$$

Furthermore, we take the radial width of an element to be equal to the mesh size, viz.

$$\Delta x = r_2 - r_1\,, \tag{2.2}$$

while the arc-length, measured at radius r_c, is given by

$$\delta s = \frac{2\pi}{n_L} r_c\,. \tag{2.3}$$

It follows then that

$$r_1 = r_c - \frac{\Delta x}{2}\,, \qquad r_2 = r_c + \frac{\Delta x}{2}\,, \tag{2.4}$$

which gives for the surface of an element ΔV_l:

$$\Delta V_l = \frac{2\pi r_c \Delta x}{n_L}\,. \tag{2.5}$$

We associate a marker point to each of the above elements and locate it equidistantly on the actual circumference of the particle (i.e. in the center of an element). At a given time those marker points are located at:

$$\mathbf{X}_l^{(d)} = \mathbf{x}_c + r_c \begin{pmatrix} \cos\left(\frac{2\pi(l-1)}{n_L} + \theta_c\right) \\ \sin\left(\frac{2\pi(l-1)}{n_L} + \theta_c\right) \end{pmatrix} \qquad \forall\ 1 \le l \le n_L \quad . \tag{2.6}$$

Due to rigid-body motion of the particle these points will have the following velocities:

$$\mathbf{U}_l^{(d)} = \mathbf{u}_c + \omega_c \times \left(\mathbf{X}_l^{(d)} - \mathbf{x}_c\right) \quad , \tag{2.7}$$

where $\mathbf{x}_c$, $\mathbf{u}_c$, ω_c, θ_c and r_c are the center locations, linear and angular velocities, angular position and radius, respectively, of a circular particle.

Remark 2.1.1 By the present arrangement the total sum of the marker volumes is independent of the number of marker elements, $\sum_l \Delta V_l = 2\pi r_c \Delta x$. This means that for $r_c >> \Delta x$ the situation is like forcing one Eulerian grid-cell in a wall-bounded flow.

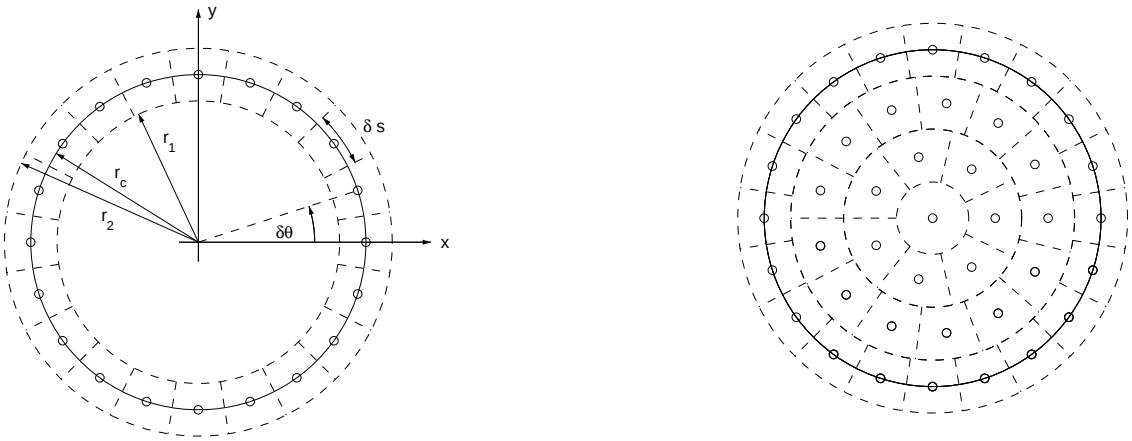

Figure 2.1: The definition of marker elements along the circumference of a circular particle (left graph): r_c is the actual circumference and small circles indicate the (equidistant) locations of marker points; element boundaries are indicated in dashed lines. The graph on the right shows how the entire solid domain can be covered by adding annuli to the interior and collocating the last marker point at the center.

REMARK 2.1.2 Other configurations are possible and have been tried (e.g. $r_2 - r_1 = \delta s$). However, the difference lies mainly in the behavior for $\delta s \neq \Delta x$ whereas we are actually interested in $\delta s \approx \Delta x$.

REMARK 2.1.3 In practice we choose the number of marker elements such that the marker volume matches the Eulerian grid cell surface as closely as possible, i.e. $\Delta V_l \approx \Delta x^2$.

REMARK 2.1.4 The inside of the solid particle can also be forced by simply adding supplementary rings of marker elements, each having a different number of elements such that for each ring $\delta_s \approx \Delta x$. As a final marker element, the remaining inner circle is defined, with the marker point being equal to the circular particle's center (cf. figure 2.1). Results from this variant are also presented below (§ 3.3.1).

REMARK 2.1.5 Extension to three dimensions, i.e. spherical particles, is relatively straightforward. In that case we would have to distribute marker points "evenly" on the surface of the sphere and associate an equal share of the surface to each; the Lagrangian volume V_l is then the product between that fraction of the surface and the shell's thickness δs.

2.2 Force formulation

What we wish to impose upon the fluid is the correct rigid-body velocity of the solid at the marker locations, i.e. we want to impose $\mathbf{U}_l^{(d)}$ at Eulerian grid nodes.

Therefore, we need to do two things:

(A) formulate an adequate volume force at the marker locations

(B) transfer that force (smoothly) to the Eulerian grid nodes.

Consider the explicit formulation (using a three-step Runge-Kutta scheme) of the momentum equation including a volume force term, written for the β-component of velocity and for grid-node

locations $\mathbf{x}_{i,j}$

$$f_\beta^k = \frac{u_\beta^k - u_\beta^{k-1}}{\Delta t} - 2\alpha_k \nu \nabla^2 u_\beta^{k-1} + 2\alpha_k \frac{\partial p^{k-1}}{\partial x_\beta} + \gamma_k [(\mathbf{u}\cdot\nabla)\mathbf{u}]_\beta^{k-1} + \zeta_k [(\mathbf{u}\cdot\nabla)\mathbf{u}]_\beta^{k-2}\,, \quad \forall \quad \mathbf{x} \in \mathbf{x}_{i,j}\,. \tag{2.8}$$

Writing the same equation—symbolically—at an arbitrary location $\mathbf{X}$ gives

$$F_\beta^k = \frac{U_\beta^k - U_\beta^{k-1}}{\Delta t} - R_\beta^k \qquad \forall \quad \mathbf{x} \in \mathbf{X}\,, \tag{2.9}$$

where R is short-hand for the collection of advection, pressure and viscous terms. The velocity U_β^k is the velocity which we wish to obtain at the end of the current time step and is therefore to be set equal to the desired velocity of the marker point: $U_\beta^k = \mathbf{U}_l^{(d)} \mathbf{i}_\beta$ ($\mathbf{i}_\beta$ is the unit vector in the direction of component β). It now remains to determine U_β^{k-1} and R_β^k from the Eulerian grid values in order to accomplish task (A). Here we propose to use Peskin's regularized delta function [7] to interpolate both quantities from the Eulerian grid to the Lagrange locations. Furthermore, we propose to use the same delta function to "spread" the resulting force F_β^k back to the Eulerian grid, quite analogous to the original immersed boundary method.

It should be noted that the interpolated terms R_β^k do not represent a proper flux balance over a marker element, but only an approximation to the expected rate-of-change of momentum at a marker location in the absence of a volume force. The only reason why we associate a volume to each marker location is for the dimensional correctness of the "spreading" (equation 2.10d below).

The algorithm for one Runge-Kutta sub-step of the projection method is the following (please refer to [1] for details of the basic time integration scheme):

$$\mathbf{r}^k = \frac{\mathbf{u}^{k-1}}{\Delta t} + 2\alpha_k \nu \nabla^2 \mathbf{u}^{k-1} - 2\alpha_k \nabla p^{k-1} - \gamma_k \left[(\mathbf{u}\cdot\nabla)\mathbf{u}\right]^{k-1} - \zeta_k \left[(\mathbf{u}\cdot\nabla)\mathbf{u}\right]^{k-2} \tag{2.10a}$$

$$\mathbf{R}^k(\mathbf{X}_l) = \sum_{i,j} \mathbf{r}^k \cdot \delta_h \left(\mathbf{x}_{i,j} - \mathbf{X}_l\right) \Delta x \Delta y\,, \tag{2.10b}$$

$$\mathbf{F}^k(\mathbf{X}_l) = \frac{\mathbf{U}^k(\mathbf{X}_l)}{\Delta t} - \mathbf{R}^k(\mathbf{X}_l)\,, \tag{2.10c}$$

$$\mathbf{f}^k(\mathbf{x}_{ij}) = \sum_l \mathbf{F}^k(\mathbf{X}_l) \cdot \delta_h \left(\mathbf{x}_{i,j} - \mathbf{X}_l\right) \Delta V_l\,, \tag{2.10d}$$

$$\frac{\mathbf{u}^* - \mathbf{u}^{k-1}}{\Delta t} = \alpha_k \nu \nabla^2 (\mathbf{u}^{k-1} + \mathbf{u}^*) - 2\alpha_k \nabla p^{k-1} - \gamma_k \left[(\mathbf{u}\cdot\nabla)\mathbf{u}\right]^{k-1} - \zeta_k \left[(\mathbf{u}\cdot\nabla)\mathbf{u}\right]^{k-2} + \mathbf{f}^k\,, \tag{2.10e}$$

$$\nabla^2 \phi^k = \frac{\nabla\cdot\mathbf{u}^*}{2\alpha_k \Delta t}\,, \tag{2.10f}$$

$$\mathbf{u}^k = \mathbf{u}^* - 2\alpha_k \Delta t \nabla \phi^k\,, \tag{2.10g}$$

$$p^k = p^{k-1} + \phi^k - \alpha_k \Delta t\, \nu \nabla^2 \phi^k\,. \tag{2.10h}$$

The spatial derivatives are evaluated by means of second-order central finite-differences on a staggered grid. Please note that the explicit r.h.s. of the momentum equations only needs to be computed once per step since we can define:

$$\mathbf{r}^k = \underbrace{\frac{\mathbf{u}^{k-1}}{\Delta t} + \alpha_k \nu \nabla^2 \mathbf{u}^{k-1} - 2\alpha_k \nabla p^{k-1} - \gamma_k \left[(\mathbf{u}\cdot\nabla)\mathbf{u}\right]^{k-1} - \zeta_k \left[(\mathbf{u}\cdot\nabla)\mathbf{u}\right]^{k-2}}_{\mathbf{h}^k} + \alpha_k \nu \nabla^2 \mathbf{u}^{k-1}\,, \tag{2.11}$$

and then re-write the Helmholtz problem (2.10e) as follows:

$$\nabla^2 \mathbf{u}^* - \frac{\mathbf{u}^*}{\alpha_k \nu \Delta t} = -\frac{1}{\nu \alpha_k} \left(\mathbf{h}^k + \mathbf{f}^k\right)\,. \tag{2.12}$$

REMARK 2.2.1 The flow field obtained by algorithm (2.10) is divergence-free in the discrete sense.

REMARK 2.2.2 Rigid-body motion in the solid domain is obtained in an approximate sense because: (a) the interpolation (2.10b) and spreading (2.10d) between Eulerian and Lagrangian positions is not exact (cf. remark 2.2.4); (b) the projection step (2.10g) introduces an additional $\mathcal{O}(\Delta t^2)$ correction.

REMARK 2.2.3 By construction the regularized delta function verifies for a uniform grid (i.e. $\Delta x = \Delta y$):

$$\sum_{i,j} \delta_h(\mathbf{x}_{i,j} - \mathbf{X})\Delta x^2 = 1\,, \tag{2.13}$$

$$\sum_{i,j} (\mathbf{x}_{i,j} - \mathbf{X}) \cdot \delta_h(\mathbf{x}_{i,j} - \mathbf{X})\Delta x^2 = 0\,, \tag{2.14}$$

for arbitrary positions $\mathbf{X}$. Both identities together give [7]:

$$\sum_{i,j} \mathbf{x}_{i,j} \cdot \delta_h(\mathbf{x}_{i,j} - \mathbf{X})\Delta x^2 = \mathbf{X}\,. \tag{2.15}$$

From (2.13) we obtain that the "spreading step" (2.10d) obeys the following equality:

$$\begin{aligned}
\sum_{i,j} \mathbf{f}(\mathbf{x}_{i,j})\Delta x^2 &= \sum_{i,j}\sum_{l} \mathbf{F}(\mathbf{X}_l) \cdot \delta_h(\mathbf{x}_{i,j} - \mathbf{X}_l)\,\Delta V_l\,\Delta x^2 \\
&= \sum_{l} \mathbf{F}(\mathbf{X}_l)\,\Delta V_l \sum_{i,j} \delta_h(\mathbf{x}_{i,j} - \mathbf{X}_l)\,\Delta x^2 \\
&= \sum_{l} \mathbf{F}(\mathbf{X}_l)\,\Delta V_l\,,
\end{aligned} \tag{2.16}$$

which means that the total force computed at the Lagrangian elements is equal to the total force applied to the computational Eulerian cells. Identity (2.15) allows us to write similarly for the torque:

$$\begin{aligned}
\sum_{i,j} \mathbf{x}_{i,j} \times \mathbf{f}(\mathbf{x}_{i,j})\Delta x^2 &= \sum_{i,j}\sum_{l} \mathbf{x}_{i,j} \times \mathbf{F}(\mathbf{X}_l) \cdot \delta_h(\mathbf{x}_{i,j} - \mathbf{X}_l)\,\Delta V_l\,\Delta x^2 \\
&= \sum_{l}\sum_{i,j} \left(\mathbf{x}_{i,j} \cdot \delta_h(\mathbf{x}_{i,j} - \mathbf{X}_l)\,\Delta x^2\right) \times \mathbf{F}(\mathbf{X}_l)\,\Delta V_l \\
&= \sum_{l} \mathbf{X}_l \times \mathbf{F}(\mathbf{X}_l)\,\Delta V_l\,,
\end{aligned} \tag{2.17}$$

and therefore (using once again identity 2.13) for the torque w.r.t. the particle center $\mathbf{x}_c$:

$$\sum_{i,j} (\mathbf{x}_{i,j} - \mathbf{x}_c) \times \mathbf{f}(\mathbf{x}_{i,j})\Delta x^2 = \sum_{l} (\mathbf{X}_l - \mathbf{x}_c) \times \mathbf{F}(\mathbf{X}_l)\,\Delta V_l\,. \tag{2.18}$$

As a consequence, it is established that the "spreading" operation from the Lagrangian to Eulerian grid does not change the total amount of force and torque which is added to the fluid. As a side-effect, it allows us to evaluate the total quantities—as needed for the integration of the Newton equation for the particle motion—either as a sum over the Lagrangian or the Eulerian contributions. From the point of view of computational efficiency, the former option is preferable.

REMARK 2.2.4 The spatial accuracy of interpolation with the discrete delta function is second-order for smooth functions [7]. By this virtue, we achieve second-order convergence of the results for Taylor-Green flow in an embedded domain (cf. § 3.1). As remarked in [3, 7] the convergence is of first order in space if the field is not smooth, e.g. at the fluid-solid interfaces. In section §3.3.1 evidence for this first-order convergence is presented in the case of flow around an oscillating cylinder.

2.3 Particular choice of the regularized delta function

We have tested two specific variants of the regularized delta function: the version with a support of 4 mesh widths of reference [7] and the more compact version (3 mesh widths) of reference [8]. Both verify the essential identities given by equations (2.13-2.14). The main interest in using the less efficient 4-point variant is for use in conjunction with collocated grid arrangements where odd-even oscillations are poorly damped. More specifically, the 4-point version of the delta function ensures that the odd grid points receive the same total amount of forcing as the even ones [7]. In the present case, both variants lead to comparable results (cf. §3.1-3.2 below).

2.4 Particle motion

The Newton equations for linear and angular momentum of a rigid body are formulated analogously to reference [1], viz.

$$V_c\,(\rho_p-\rho_f)\,\dot{\mathbf{u}}_c \;=\; -\rho_f \underbrace{\sum_l \mathbf{F}(\mathbf{X}_l)\,\Delta V_l}_{\mathcal{F}} + (\rho_p-\rho_f)\,V_c\,\mathbf{g}\,, \tag{2.19a}$$

$$V_c\,\frac{r_c^2}{2}\,\rho_p\,\dot{\omega}_c \;=\; -\rho_f \underbrace{\sum_l (\mathbf{X}_l-\mathbf{x}_c)\times\mathbf{F}(\mathbf{X}_l)\,\Delta V_l}_{\mathcal{T}} + \rho_f \frac{\mathrm{d}}{\mathrm{d}t}\underbrace{\int_{\mathcal{S}} (\mathbf{r}\times\mathbf{u})\;\mathrm{d}V}_{\mathcal{I}}\,. \tag{2.19b}$$

The second term on the r.h.s. of (2.19b) represents the rate of change of angular momentum inside the solid domain and stems from the fact that the flow inside the solid domain does in general not exactly satisfy the rigid-body constraint if forcing is only applied along the circumference of the particle.

For the present scheme, the sum of the hydrodynamic forces over one full time step is equal to the sum of the forces at each Runge-Kutta sub-step, i.e. $\mathbf{F}^1+\mathbf{F}^2+\mathbf{F}^3$ (cf. [1, § A.2.2]). Therefore, a Runge-Kutta integration which is consistent with the time integration of the fluid can be written as follows:

$$\frac{\mathbf{u}_c^k-\mathbf{u}_c^{k-1}}{\Delta t} \;=\; -\frac{\rho_f}{V_c(\rho_p-\rho_f)}\,\mathcal{F}^k + 2\alpha_k\mathbf{g}\,, \tag{2.20a}$$

$$\frac{\mathbf{x}_c^k-\mathbf{x}_c^{k-1}}{\Delta t} \;=\; \alpha_k\left(\mathbf{u}_c^k+\mathbf{u}_c^{k-1}\right)\,, \tag{2.20b}$$

$$\frac{\omega_c^k-\omega_c^{k-1}}{\Delta t} \;=\; -\frac{\rho_f}{V_c\frac{r_c^2}{2}\rho_p}\,\mathcal{T}^k + \frac{\rho_f}{V_c\frac{r_c^2}{2}\rho_p}\,\frac{\left(\mathcal{I}^k-\mathcal{I}^{k-1}\right)}{\Delta t}\,, \tag{2.20c}$$

$$\frac{\theta_c^k-\theta_c^{k-1}}{\Delta t} \;=\; \alpha_k\left(\omega_c^k+\omega_c^{k-1}\right)\,, \tag{2.20d}$$

where the angular position θ is actually not strictly needed in the present case.

The basic scheme consists in first solving equations (2.10) with the particle positions and velocities known from the previous Runge-Kutta level and then solving equations (2.20) as indicated, using the most recent flow field. This way of coupling the two systems is called "weak coupling" or "staggered scheme" or simply "explicit" (not to be confused with the type of solution of the flow equations, which is semi-implicit in the present case).

It has been noted by various authors [9, 10] that the treatment of very light particles presents a problem for methods where the fluid equations are "weakly" coupled to the equations of motion for the rigid particles. We have found that a density ratio of $\rho_p/\rho_f \approx 1.05$ is a lower limit for stable explicit integration of the fluid-particle system when using the present method. We have observed that this limit does not depend significantly upon the chosen time step.

Please note that a limit of $\rho_p/\rho_f \approx 1.9$ was observed in [1] for stable integration of the "weakly" coupled method of reference [6].

2.4.1 Iterative coupling

When imposing rigid-body motion *throughout* the solid domain (as presented in § 3.3.1 below), we find that the explicitly coupled procedure is either unstable ($\rho_p/\rho_f \leq 1.7$) or the interaction forces oscillate in time. This behavior is probably due to the additional inertia of the fluid mass inside the solid volume.

Therefore, we use an iterative method in this case. Particle motion and fluid motion are iterated for each Runge-Kutta sub-step until the particle motion converges. In order to simplify the notation, consider the following two coupled sub-systems where each contains only one variable, flow velocity $\mathbf{u}$ and particle center velocity $\mathbf{u}_c$, respectively:

$$\mathbf{u}^k = \mathbf{u}^{k-1} + \Psi_1\left(\mathbf{u}^k, \mathbf{u}^{k-1}, \mathbf{u}^{k-2}, \mathbf{u}_c^{k-1}\right) , \tag{2.21a}$$

$$\mathbf{u}_c^k = \mathbf{u}_c^{k-1} + \Psi_2\left(\mathbf{u}_c^{k-1}, \mathbf{u}^{k-1}, \mathbf{u}^{k-2}\right) , \tag{2.21b}$$

and the functions Ψ_1, Ψ_2 represent the time advancement of each subsystem. This model is representative of our full system inasmuch as it is implicit in the former case and explicit in the latter. It can directly be transferred and applied to the full equations.

An iterative solution similar to Gauss-Seidel in linear algebra can be obtained by stepping the following system

$$\tilde{\mathbf{u}}^{it} = \mathbf{u}^{k-1} + \Psi_1\left(\mathbf{u}^{it}, \mathbf{u}^{it-1}, \mathbf{u}^{k-2}, \mathbf{u}_c^{it-1}\right) , \tag{2.22a}$$

$$\tilde{\mathbf{u}}_c^{it} = \mathbf{u}_c^{k-1} + \Psi_2\left(\mathbf{u}_c^{it-1}, \mathbf{u}^{it}, \mathbf{u}^{k-2}\right) , \tag{2.22b}$$

alternatingly until convergence (it is the iteration counter). Please note that exchanging $\mathbf{u}^{it}$ for $\mathbf{u}^{it-1}$ in (2.22b) would turn the method into a Jacobi-type method. Additionally, under-relaxation was performed for all variables in the following manner:

$$\mathbf{u}^{it} = \omega_{relax}\,\tilde{\mathbf{u}}^{it} + (1-\omega_{relax})\,\mathbf{u}^{it-1} \quad . \tag{2.23}$$

The value $\omega_{relax} = 0.5$ was used in all cases.

In practice we measure the convergence by comparing the maximum of the increments of linear and angular position and velocity, normalized as follows:

$$\max\left\{ \frac{|\mathbf{x}_c^{it} - \mathbf{x}_c^{it-1}|}{r_c}, \quad \frac{|\mathbf{u}_c^{it} - \mathbf{u}_c^{it-1}|}{\sqrt{|\mathbf{g}|\,r_c}}, \quad \frac{|\theta_c^{it} - \theta_c^{it-1}|}{2\pi}, \quad \frac{|\omega_c^{it} - \omega_c^{it-1}|}{\sqrt{|\mathbf{g}|/r_c}} \right\} \leq \varepsilon \quad , \tag{2.24}$$

where the tolerance ε was set to 10^{-5} and the maximum is taken over all particles.

REMARK 2.4.1 The above iterative scheme could immediately be used in order to treat extremely light particles with our present scheme ($\rho_p/\rho_f \leq 1.05$) although this has not been tried in practice.

Chapter 3

Results

3.1 Taylor-Green vortices

Here we simulate the decay of Taylor-Green vortices inside a sub-domain embedded within the computational domain. The initial field is identical to the exact solution given by

$$u(x,y,t) = \sin(k_x x)\cos(k_y y)e^{-(k_x^2+k_y^2)\nu t}, \tag{3.1a}$$

$$v(x,y,t) = -\frac{k_x}{k_y}\sin(k_y y)\cos(k_x x)e^{-(k_x^2+k_y^2)\nu t}, \tag{3.1b}$$

$$p(x,y,t) = \frac{1}{2}\left(\cos^2(k_y y)\frac{k_x^2}{k_y^2} - \sin^2(k_x x)\right)e^{-2(k_x^2+k_y^2)\nu t}, \tag{3.1c}$$

which also provides the time-dependent boundary conditions at the computational domain and the time-dependent velocity values to be prescribed at the interface of the embedded sub-domain.

The computational domain has the dimension $\Omega = [-1.5, 1.5] \times [-1.5, 1.5]$. The sub-domain consists of a circle with center position (0,0) and radius unity.

The viscosity is set to $\nu = 0.2$ which gives a value for the Reynolds number based on vortex size and maximum velocity of 10. The equations are advanced from $t_0 = 0$ until $t_{fin} = 0.3$ using a time step of $\Delta t = 0.001$. This parameters set is equal to the case considered in reference [5].

Figure 4.1 shows the spatial convergence of velocity to be second order when no embedded object is present, i.e. for our basic fluid code. Figure 4.2 shows the convergence of the velocity inside the embedded sub-domain (i.e. for nodes which satisfy $|\mathbf{x}_{i,j}| < 1$) as a function of the number of grid nodes in the entire domain. It can be seen that the convergence remains second order with the present forcing method. The compact three-point regularized delta function leads to lower errors.

It is noteworthy that the error does not depend strongly upon the position of the immersed boundary relative to the grid. This feature is demonstrated in table 3.1 where the error is plotted for a fixed resolution and the circular sub-domain was shifted horizontally by various fractions of the mesh-width. The different results could be barely distinguished on a logarithmic scale such as the one used for figure 4.1.

3.2 Flow around a fixed cylinder

Here we consider the flow around a stationary cylinder with diameter D located at the origin in a domain which measures $\Omega = [-6.17, 20.5]D \times [-13.33, 13.33]D$. The uniform grid has 512×512 nodes, i.e. $D/\Delta x = 19.2$. Two values for the Reynolds number $Re_D = \frac{u_\infty D}{\nu}$ were chosen: 100, 185. In the former case, the time step was $\Delta t = 0.005$, in the latter $\Delta t = 0.003$, both leading to a maximum CFL number of approximately 0.5.

$x_c/\Delta x$	4-point δ_h [7]	3-point δ_h [8]
0.0	0.003906	0.002181
0.1	0.003919	0.002287
0.2	0.003904	0.002355
0.354	0.003849	0.002365
0.4	0.003864	0.002346

Table 3.1: Maximum error of the velocity in the case of Taylor-Green vortices computed in an immersed circular domain. The global grid has 61 nodes, i.e. $\Delta x = 0.05$. The center of the circular subdomain was shifted horizontally by various fractions of the mesh width. Results are shown for the two different variants of the regularized delta function.

	$Re_D = 100$			$Re_D = 185$		
method	C_D	C_L	St	C_D	$(C_L)_{rms}$	St
present, 4-point δ_h	1.516 ± 0.011	± 0.345	0.169			
present, 3-point δ_h	1.503 ± 0.011	± 0.352	0.170	1.464 ± 0.042	0.478	0.198
$\sim$, forcing throughout				1.402 ± 0.038	0.461	0.196
immersed boundary	1.447 ± 0.010	± 0.358	0.169			
Kajishima	1.427 ± 0.009	± 0.334	0.171			
reference	$1.350 \pm 0.012^*$	$\pm 0.339^*$	0.165^*	$1.22^\dagger$	$0.422^\dagger$	$0.195^\dagger$

Table 3.2: Dimensionless coefficients obtained from the simulation of the flow around a stationary cylinder using the present method, the immersed boundary method and Kajishima's method using a 512×512 uniform grid and a time step of $\Delta t = 0.005$ ($Re_D = 100$), $\Delta t = 0.003$ ($Re_D = 185$). The reference values correspond to: * numerical computation of Liu *et al.* [11]; † numerical computation of Lu and Dalton [12].

The boundary conditions are uniform velocity at the inflow and along the top and bottom boundaries; a convective outflow condition was used.

Table 3.2 shows the resulting drag, lift and oscillation frequencies as compared to data from the literature. The agreement is generally very good for the present method with either variant of the delta function, for the immersed boundary method and for the method of Kajishima. The mean drag is consistently over-predicted in our computations, which is due to the effect of confinement in our relatively small domain. Additional runs with higher spatial resolution in the same domain confirmed the numbers in the table (1024×1024 points, $\Delta t = 0.003$, $Re_D = 100$, present method with 4-point δ_h: $C_D = 1.541 \pm 0.011$, $C_L = \pm 0.330$, $St = 0.172$).

3.3 Flow around an oscillating cylinder

The cylinder now follows a prescribed periodic motion perpendicular to the mean flow, i.e.:

$$y_c(t) = A \sin(2\pi f_f t)\,, \tag{3.2}$$

with the amplitude set to $A = 0.2D$ and the frequency $f_f/f_n = 0.8$, where f_n is the natural shedding frequency obtained from the value of the Strouhal number from the literature: $St = f_n D/u_\infty = 0.195$ (for $Re_D = 185$). This case corresponds to one of the cases simulated in reference [12]. The maximum velocity of the cylinder is $\max(|\mathbf{u}_c|)/u_\infty = 2\pi f_f A/u_\infty = 0.196$.

The domain size is the same as above (§ 3.2) and the grid dimension was 512×512 (1024×1024) with a time step of $\Delta t = 0.003$ leading to a maximum value for the CFL number of $CFL \leq 0.3$ ($CFL \leq 0.6$).

Table 3.3 shows the mean drag as well as the fluctuation amplitudes of drag and lift. Compared to the values of reference [12] our results again show a systematic over-prediction of the mean drag as noted in the case of the stationary cylinder and attributed to the confinement in a rather small domain. The r.m.s. value of the lift coefficient obtained by our present method is in good agreement with the reference value. It can also be seen that the result obtained by using the coarser grid of 512×512 nodes is not yet converged in terms of the lift coefficient.

The amount of energy transferred between fluid and cylinder over one period T of the translational oscillation can be defined as [13]:

$$E = \int_0^T \frac{\dot{y}_c}{D} C_L \mathrm{d}t \,. \tag{3.3}$$

Work is done on the cylinder when the quantity E is positive. There is a general agreement of all tested methods that for this case, E takes small positive values (cf. table 3.3).

Figure 4.3 shows that the temporal variations of drag and lift are reasonably smooth periodic curves when using the current scheme. Unfortunately the corresponding plots are not provided in reference [12]. The lift and drag variation obtained by the immersed boundary method (figure 4.4) exhibit a more or less smooth behaviour, depending upon the choice of the feedback parameters. Figure 4.5 gives the phase-space plots obtained through the method of Kajishima and Takiguchi [6] implemented as shown in [1]. Significant oscillations on the time-scale of the mesh-width divided by the cylinder velocity are observed, i.e. in the case of the 1024×1024 grid, 16 strong peaks are recognizable in the C_D and—to a lesser extent—C_L orbits of figure 4.5 as the cylinder traverses $16\Delta x$ over half a period.

Figure 4.6 shows a close-up of the velocity field near the solid body obtained by the present method. It can be seen that there is a vortex-dipole-like motion inside the solid particle. Near the particle's circumference, the no-slip condition is enforced.

3.3.1 How well can rigid-body motion be imposed?

Here we consider the efficiency of the present method in imposing a rigid-body motion upon the flow field. For this purpose, we distribute marker elements *throughout* the surface of the circular cylinder, as mentioned in remark 2.1.4 (cf. figure 2.1). Please note that the number of marker points/elements is thereby increased from 60 to 315 in the present case (120 to 1206 for the fine grid of 1024×1024 nodes) with the corresponding (linear) increase in computing time.

method	grid	C_D	$(C_L)_{rms}$	E
present	512×512	1.339 ± 0.064	0.247	0.0524
	1024×1024	1.380 ± 0.063	0.176	0.0407
present, forcing throughout	512×512	1.301 ± 0.067	0.312	0.0671
	1024×1024	1.302 ± 0.058	0.240	0.0623
immersed boundary	1024×1024	1.317 ± 0.068	0.305	0.1009
Kajishima	1024×1024	1.282 ± 0.088	0.223	0.0545
reference†		1.25	0.18	

Table 3.3: Dimensionless coefficients obtained from the simulation of the flow around an oscillating cylinder at $Re_D = 185$ using the present method with the 3-point δ_h of [8], the immersed boundary method (parameters: $\kappa 10^5$, $\gamma = 10$, $\Delta t = 0.0005$) and the method of Kajishima and Takiguchi [6] implemented in divergence-free manner as shown in [1]. The time step was $\Delta t = 0.003$. E is the energy transfer defined in the text. †Values from [12].

Figure 4.8 also shows the deviation from rigid-body motion measured at pressure node-points inside the circular cylinder as a function of the phase angle of the forced motion. (Measuring the deviation at the staggered grid-nodes individually for each velocity component leads to smaller values due to the second-order interpolation error). The deviation is presented in a root-mean-square sense and normalized with the free-stream velocity. It can be seen that the deviation is less than 4% for all cases, oscillating with the grid-traverse frequency and having a quiescent phase around the extrema of the trajectory, i.e. when the cylinder has the lowest velocity. Reducing the time step by a factor of 10 does not have a large effect (the deviations are only reduced by a around 20%), probably because the spatial error is dominant at this resolution. Grid refinement, on the other hand, by a factor of 2 leads to a reduction of approximately 50%. This observation implies that the convergence properties of the present scheme are of first order in space for discontinuous fields (cf. §3.1 for second-order convergence in the case of a smooth field). Lai and Peskin [3] observed the same convergence properties in the framework of the original immersed boundary method.

Figure 4.9 shows a close-up of the velocity field around the oscillating cylinder when forcing the entire solid domain. It can be seen that the deviation from rigidity is mainly concentrated close to the leading edge of the cylinder where the normal gradients are expected to be largest.

3.4 Sedimentation of a single particle

A single particle is accelerating from rest due to the action of gravity in an initially ambient fluid, bounded by no-slip walls on all sides of the domain. Since we are presently not concerned with direct particle-wall interactions, we do not consider the rebound of the particle from the bottom boundary.

We study two cases with different particle densities.

3.4.1 Light particle

This case corresponds to the one computed in [14, § 8.3.3]. The physical parameters of the problem are the following:

- domain size $\Omega = [0, 6] \times [-1, 1]$;
- disc radius $r_c = 0.125$;
- initial location of the disc $\mathbf{x}_c = (2, 0.001)$ (small lateral offset in order to trigger the particle's wake instability);
- density ratio $\rho_p/\rho_f = 1.5$;
- fluid viscosity $\nu = 0.01$;
- gravitational acceleration $\mathbf{g} = (981, 0)$.

The maximum Reynolds number takes a value of $Re_D \approx 330$ in this case. The numerical parameters as used in all our computations were:

- mesh width $\Delta x = 1/256$, i.e. $2r_c/\Delta x = 64$ and $N_x = 1537$, $N_y = 513$;
- time step $\Delta t = 0.0001$ (except otherwise stated), which leads to a maximum CFL number around 0.65.

We consider results obtained by the following methods:

(A) The present method. Forcing is only applied to the circumference of the particle.

(B) The present method. Forcing is applied to the entire solid domain. Iterative coupling of fluid and particle equations is necessary for this method in the present case. The number of sub-iterations varied between 5 and 12.

(C) The immersed boundary method as implemented in [1]. The spring stiffness was set to $\kappa = 10^7$, the damping to $\gamma = 100$ which leads to deviations from circular shape of less than $0.004\, r_c$. This set of parameters implied the use of the time step $\Delta t = 0.0001$. Please refer to § 3.4.2 for a further discussion of the choice of these parameters.

(D) The method of reference [14]. These results were re-computed and provided by T.-W. Pan, University of Houston.

Figure 4.10 shows the history of the center velocity and position in the direction of gravity. The agreement between all three methods implemented in our finite-difference framework is generally very close; compared to T.-W. Pan's results, the velocity is systematically higher by around 6%. The maximum Reynolds numbers are: (A) 329.87, (B) 336.15, (C) 333.21, (D) 311.74. The discrepancy could be due to a larger time step used by T.-W. Pan or related to the basic spatial discretization.

Figure 4.11 shows position and velocity in the direction perpendicular to gravity, figure 4.12 the angular velocity. A lateral motion of the particle within the current domain is only observed if the initial position is chosen non-symmetric w.r.t. the grid since our spatial scheme fully preserves the symmetry and perturbations (e.g. caused by round-off) do not grow fast enough. With the current offset by $\Delta x/4$ (similarly for other values; not shown) lateral motion sets in quickly, albeit to a much lesser extent than exhibited by the results provided by T.-W. Pan. We believe that the non-symmetric triangular grid used therein is responsible for the larger lateral motion as well as for the higher angular velocity. Focussing on our own three data-sets, we observe that the IB method yields the largest deviation from a vertical trajectory.

Influence of the time step. Here we consider results obtained by the present method while varying the time step. Figures 4.13- 4.15 show the results for $\Delta t = 0.00025$, $\Delta t = 0.0001$ (as used in previous figures) and $\Delta t = 0.00005$ which lead to respective values of the CFL number of approximately 1.5, 0.65 and 0.33. From these figures the temporal convergence is evident.

3.4.2 Heavy particle

The physical parameters of the problem are the following:

- domain size $\Omega = [0, 6] \times [-0.5, 0.5]$;
- disc radius $r_c = 0.1$;
- initial location of the disc $\mathbf{x}_c = (0.4, 0)$;
- density ratio $\rho_p/\rho_f = 8$;
- fluid viscosity $\nu = 0.005$;
- gravitational acceleration $\mathbf{g} = (9.81, 0)$.

The maximum Reynolds number takes a value of $Re_D \approx 150$ in this case. The numerical parameters as used in all our computations were:

- mesh width $\Delta x = 1/300$, i.e. $2r_c/\Delta x = 60$ and $N_x = 1801$, $N_y = 301$;
- time step $\Delta t = 0.0005$, which leads to a maximum CFL number around 0.75.

We consider results obtained by the following methods:

(A) The present method. Forcing is only applied to the circumference of the particle.

(B) The present method. Forcing is applied to the entire solid domain and iterative coupling between fluid and particle equations is used. The number of sub-iterations varied between 5 and 10.

(C) The immersed boundary method as implemented in [1]. The parameters for the spring stiffness $\kappa = 2 \cdot 10^5$ and the damping $\gamma = 50$ were used along with the reduced time step of $\Delta t = 0.0002$. These values were further varied as indicated below.

(D) The method of Kajishima [6] as implemented in a divergence-free manner in [1].

Figure 4.16 shows the history of the center velocity and position in the direction of gravity. There is a general agreement of all four results to within 3.5% for the center-velocity. The maximum Reynolds numbers are: (A) 144.68, (B) 149.70, (C) 147.50, (D) 149.96. It should be noted that the lateral position and velocity as well as the angular particle motion are not shown because no significant values are obtained for this symmetric case.

A comparison of the sum of the hydrodynamic forces in the direction of gravity, $\sum_l \mathbf{F}_l \mathbf{g}/|\mathbf{g}|$, is shown in figures 4.17- 4.18. It can be observed that only the method of reference [6] features significant oscillations during the particle's traverse of the stationary grid, consistent with our observations in the oscillating cylinder case.

Free parameters of the immersed boundary method. Figure 4.19 shows data which explains the problems associated with choosing acceptable values for the free parameters in the immersed boundary method. On the left graph we have plotted the maximum deviation of a Lagrangian marker point's position w.r.t. its desired position over time. The maximum is taken over all marker points and the result is normalized by the particle's radius. It can be seen that the spring stiffness has to be adjusted to a value in the range of $2 \cdot 10^5 \leq \kappa \leq 10^6$ in order to obtain a maximum deviation of less than 1%. However, at the same time the time step needs to be reduced to $\Delta t = 0.0002$ for reasons of stability. On the other hand, the damping parameter γ needs to be set to a finite value in order to prevent oscillations of the hydrodynamic force, particularly during the start-up of the particle motion and to a lesser extent during the later stages. The plot on the right of figure 4.19 shows the history of the sum of the vertical force for different choices of the parameters. In the present case, a value of $\kappa \geq 50$ seems to lead to an acceptable behavior of the force (except for very early times). Increasing the damping further to $\gamma = 200$ while keeping a constant value for the stiffness (not shown) requires an additional reduction of the time step to $\Delta t = 0.00005$ ($CFL \approx 0.075$). We feel that the necessary "tuning" of the indirect force parameters and the implications for the allowable time step are a serious drawback of the immersed boundary method.

3.5 Drafting-kissing-tumbling case

Two particles with identical density and radius are accelerating from rest in an ambient fluid. Initially, they have the same horizontal position, but some vertical offset. The trailing particle catches up with the leading one due to the reduced drag in the former particle's wake. This case has frequently been considered in the literature (e.g. [9, 14–16]). Here, we will consider the density ratio $\rho_p/\rho_f = 1.5$ for which data from reference [14] is available.

Furthermore, the present case involves particle-particle interaction, i.e. the particles approach each other closely, albeit probably not closely enough for collision/film rupture to take place. However, very thin liquid inter-particle films cannot be resolved by a typical grid and therefore the correct build-up of repulsive pressure is not captured which can lead to possible (partial) "overlap" of the particle positions in the numerical computation. In practice, various authors use artificial repulsion potentials which prevent such non-physical situations [9, 14, 17]. The formulation of a model for treating inter-particle collisions lies outside the scope of the present note. Therefore, we will stop our computations when the particle distance is smaller than two mesh widths, say.

This case corresponds to the one computed in [14, § 8.4]. The physical parameters of the problem are the following:

- domain size $\Omega = [0, 6] \times [-1, 1]$;
- disc radius $r_c^{(1)} = r_c^{(2)} = 0.125$;
- initial location of the discs is $\mathbf{x}_c^{(1)} = (1, 0.001)$, $\mathbf{x}_c^{(2)} = (1.5, 0.001)$ (the small lateral offset is again introduced in order to trigger the particle's wake instability);

- density ratio $\rho_p^{(1)}/\rho_f = \rho_p^{(2)}/\rho_f = 1.5$;
- fluid viscosity $\nu = 0.01$;
- gravitational acceleration $\mathbf{g} = (981, 0)$.

The numerical parameters as used in all our computations were:

- mesh width $\Delta x = 1/256$, i.e. $2r_c/\Delta x = 64$ and $N_x = 1537$, $N_y = 513$;
- time step $\Delta t = 0.0001$ (except otherwise stated), which leads to a maximum CFL number around 0.85.

We consider results obtained by the following methods:

(A) The present method. Forcing is only applied to the circumference of the particle.

(B) The immersed boundary method as implemented in [1]. The spring stiffness was set to $\kappa = 10^7$, the damping to $\gamma = 100$ as in § 3.4.1.

(D) The method of reference [14]. These results were re-computed and provided by T.-W. Pan, University of Houston.

Figures 4.20-4.23 show our present results as well as the ones kindly re-computed and provided by T.-W. Pan, University of Houston. The latter results are, therefore, not exactly equivalent to those of reference [14].

For the vertical position and velocity, we observe a very close agreement of all three results. The horizontal position and velocity, on the other hand, differ considerably between our computations and the data of Pan; particularly, a much more pronounced lateral motion is observed in the latter data-set (cf. the discussion in § 3.4.1). A similar discrepancy was already noted in [15], where the authors attributed the systematic "drift" of the particles towards the positive horizontal direction to the triangular mesh used in reference [14].

Finally, we observe that in this case the IB method leads to stronger particle rotation than the present method. The origin for this behavior is not known at the present time.

3.6 Particle-wake interaction case

Two particles with a vertical and horizontal offset are accelerating from rest. The "trailing" particle has a higher density than the leading and therefore passes the leading particle, subjecting it to perturbations due to its wake. This case does not involve direct particle-particle interactions because the minimum distance between particles is much larger than the mesh width. Therefore, no collision model is needed which makes this case attractive as a "benchmark" for testing the basic fluid-solid interaction method. Again the computation is stopped before the heavier particle reaches the bottom boundary of the computational domain.

The physical parameters of the problem are the following:

- domain size $\Omega = [0, 10] \times [-1, 1]$;
- disc radius $r_c^{(1)} = r_c^{(2)} = 0.1$;
- initial location of the discs $\mathbf{x}_c^{(1)} = (0.8, -0.13)$, $\mathbf{x}_c^{(2)} = (1.2, +0.13)$;
- density ratio $\rho_p^{(1)}/\rho_f = 1.4$, $\rho_p^{(2)}/\rho_f = 1.05$;
- fluid viscosity $\nu = 0.0008$;
- gravitational acceleration $\mathbf{g} = (9.81, 0)$.

The values for the numerical parameters were the following:

- mesh width $\Delta x = 1/200$, i.e. $2r_c/\Delta x = 40$ and $N_x = 2001$, $N_y = 401$;
- time step $\Delta t = 0.0015$, which leads to a maximum CFL number around 0.5.

The final time shown below is $t_{fin} = 9.7$, corresponding to the center of the heavy particle being located at $4r_c$ above the bottom boundary. The maximum Reynolds numbers recorded during the simulation were $Re_D^{(1)} = 250.00$, $Re_D^{(2)} = 170.97$.

Figure 4.24 shows the trajectories of the two particles and figure 4.25 several snapshots of the vorticity field. It can be observed that the heavier particle follows a slightly undulating path due to the time-varying horizontal force induced by its own alternate vortex shedding. On the other hand, the deviation of the lighter particle's path from a vertical one is mainly determined by the wake of the heavier particle. Therefore, the former particle's lateral excursions are much more pronounced. A close look at figure 4.26 reveals that the light particle is even swept upwards during a short period, approximately at the time when both particles are closest. It is noteworthy that the heavy particle's vertical velocity reaches its maximum value and then slightly decelerates when vortex shedding has reached a periodic state.

The further plots of horizontal position and velocity, angular position and velocity and hydrodynamic forces shown in figures 4.27-4.29 speak for themselves. Finally, the torque as shown in figure 4.30 shows oscillations around a well-defined curve. This is a quantity which is seldom shown in the literature. We would like to point out that the absolute value is rather small and that the curves for angular velocity and angle are still perfectly smooth. The largest angular motion (in radians) during the simulation is $\max|\theta_c^{(1)}| = 0.085$ and $\max|\theta_c^{(2)}| = 0.363$.

3.7 A note on efficiency

Operation count. The following numbers refer to the operations carried out during one Runge-Kutta sub-step, of which there are three per full time step. The main work in the pure fluid part of the code is done while solving the two Helmholtz problems during the prediction step (2.10e) and when solving the Poisson problem of the projection step (2.10f). When using a direct, cyclic reduction method such as implemented in FISHPACK, the asymptotic operation count is $\mathcal{O}(N_x N_y \log(N_x))$ each. On the other hand, the solution of the Newton equations for N_p particles requires simply $\mathcal{O}(N_p)$ operations. Finally, the fluid-solid interaction requires twice the evaluation of sums over the Lagrangian marker elements (as a by-product yielding the value for the sum of the hydrodynamic forces) and the stencil size $n_{\delta_h} = 3$ of the regularized delta function [8], i.e. $\mathcal{O}(N_p\, n_{\delta_h}^2\, r_p/\Delta x)$ operations, supposing that the markers are distributed along the circumference of the interface with a spacing equal to the mesh-width. The ratio between particle radius and mesh width depends on the Reynolds number. (In practice, Kajishima and Takiguchi use as little as $r_p/\Delta x = 5$ for Reynolds numbers up to 400.) As a consequence, if we introduce a characteristic macroscopic length-scale $L = N_x \Delta x$, the overall scaling of the code with the number of particles depends on the ratio of the two length scales, viz. $\mathcal{O}(N_p + N_x^2 \log(N_x) + N_p n_{\delta_h}^2 N_x r_p/L)$. In other words, for large domains and moderate particle counts, the fluid part will dominate.

Timing. Table 3.4 shows some execution times per time step for the present scheme. It can be seen that for a 1024×1024 grid and using 100 Lagrangian markers per particle the difference between the pure fluid code and simulating 1000 particles is less than 60%.

Time step. It was shown above that the present method does not have a noticeable influence upon the allowable time step, when expressed in terms of the CFL condition. This does not mean, however, that the largest time step should be chosen in a practical computation because of the temporal discretization error. If we take the result of § 3.4.1 as a guide, then a value of $CFL \approx 0.5$ seems reasonable.

Parallelization. The potential for parallelizing the present algorithm can be gauged by comparison with the parallelized version of the immersed boundary code presented in reference [2]. Therein a domain decomposition method for the fluid part, using an ADI method for the Helmholtz

$N_x \times N_y$	N_p	n_L	$t_{exec}[sec]$
512×512	0	–	1.72
1024×1024	0	–	7.39
1024×1024	1	100	7.39
1024×1024	1	200	7.43
1024×1024	1	400	7.71
1024×1024	10	100	7.74
1024×1024	100	100	8.09
1024×1024	1000	100	11.55

Table 3.4: Execution time (per full time step) of the present scheme on an Intel Pentium-4 system running at 3GHz clock speed, 64 bit arithmetic, using the FISHPACK library and the GNU Fortran compiler (`-O3`). The parameters are: grid size $N_x \times N_y$, number of particles N_p, number of Lagrange markers per particle n_L.

equations and a multi-grid method for the Poisson equation, and a particles-in-sub-domain association for allocating particles to different processors was implemented and shown to offer good results for coarse-grained simulations. In three space dimensions, the potential speed-up is expected to be even better since for a given number of processors, more individual work needs to be done.

Chapter 4

Conclusion

We have presented a new variant of a fictitious domain method with a direct formulation of the fluid-solid interaction force. The regularized delta function of Peskin and co-workers [3, 7, 8] is used for the association between arbitrary Lagrangian and discrete Eulerian positions. Thereby, the hydrodynamic forces acting upon the solid domains, which are at the same time driving the particle motion, are free from significant oscillations.

The current method was weakly coupled to the Newton equations for the rigid-body motion of the particles and as a lower limit for the density ratio a value of $\rho_p/\rho_f \approx 1.05$ was observed for stable integration.

The new scheme was applied to Taylor-Green flow, flow around fixed and oscillating cylinders as well as sedimentation problems. The comparison with reference values from the literature as well as comparisons with our own computations using the original IB method and the direct method of reference [6] shows very satisfactory results.

Taking into account the fast execution speed of the current method we can conclude that it is indeed very competitive. Extension to three space dimensions is currently underway.

Acknowledgements

I am grateful to T.W. Pan for providing his numerical results for comparison.

Bibliography

[1] M. Uhlmann. First experiments with the simulation of particulate flows. Technical Report No. 1020, CIEMAT, Madrid, Spain, 2003. ISSN 1135-9420.

[2] M. Uhlmann. Simulation of particulate flows on multi-processor machines with distributed memory. Technical Report No. ?, CIEMAT, URL: `www.ciemat.es/sweb/comfos/personal/uhlmann/particle/report/report2.pdf`, Madrid, Spain, 2003.

[3] M.-C. Lai and C.S. Peskin. An immersed boundary method with formal second-order accuracy and reduced numerical viscosity. *J. Comput. Phys.*, 160:705–719, 2000.

[4] E.A. Fadlun, R. Verzicco, P. Orlandi, and J. Mohd-Yusof. Combined immersed-boundary finite-difference methods for three-dimensional complex flow simulations. *J. Comput. Phys.*, 161:35–60, 2000.

[5] J. Kim, D. Kim, and H. Choi. An immersed-boundary finite-volume method for simulations of flow in complex geometries. *J. Comput. Phys.*, 171:132–150, 2001.

[6] T. Kajishima and S. Takiguchi. Interaction between particle clusters and particle-induced turbulence. *Int. J. Heat Fluid Flow*, 23:639–646, 2002.

[7] C.S. Peskin. The immersed boundary method. *Acta Numerica*, pages 1–39, 2002.

[8] A.M. Roma, C.S. Peskin, and M.J. Berger. An adaptive version of the immersed boundary method. *J. Comput. Phys.*, 153:509–534, 1999.

[9] H.H. Hu, N.A. Patankar, and N.Y. Zhu. Direct numerical simulation of fluid-solid systems using the arbitrary Lagrangian Eulerian technique. *J. Comput. Phys.*, 169:427–462, 2001.

[10] M. Jenny, G. Bouchet, and J. Dušec. Nonvertical ascension or fall of a free sphere in a Newtonain fluid. *Phys. Fluids*, 15(1):L9–L12, 2003.

[11] C. Liu, X. Zheng, and C.H. Sung. Preconditioned multigrid methods for unsteady incompressible flows. *J. Comput. Phys.*, 139:35–57, 1998.

[12] X.Y. Lu and C. Dalton. Calculation of the timing of vortex formation from an oscillating cylinder. *J. Fluids Structures*, 10(527-541), 1996.

[13] H.M. Blackburn and R.D. Henderson. A study of two-dimensional flow past an oscillating cylinder. *J. Fluid Mech.*, 385:255–286, 1999.

[14] R. Glowinski, T.W. Pan, T.I. Hesla, D.D. Joseph, and J. Périaux. A ficticious domain approach to the direct numerical simulation of incompressible viscous flow past moving rigid bodies: Application to particulate flow. *J. Comput. Phys.*, 169:363–426, 2001.

[15] Z. Zhang and A. Prosperetti. A method for particle simulation. *J. Appl. Mech.*, 70:64–74, 2003.

[16] Z.-G. Feng and E.E. Michaelides. The immersed boundary-lattice Boltzmann method for solving fluid-particles interaction problems. *J. Comput. Phys.*, 2004. In press.

[17] K. Höfler and S. Schwarzer. Navier-Stokes simulation with constraint forces: Finite-difference method for particle-laden flows and complex geometries. *Phys. Rev. E*, 61(6):7146–7160, 2000.

Figures

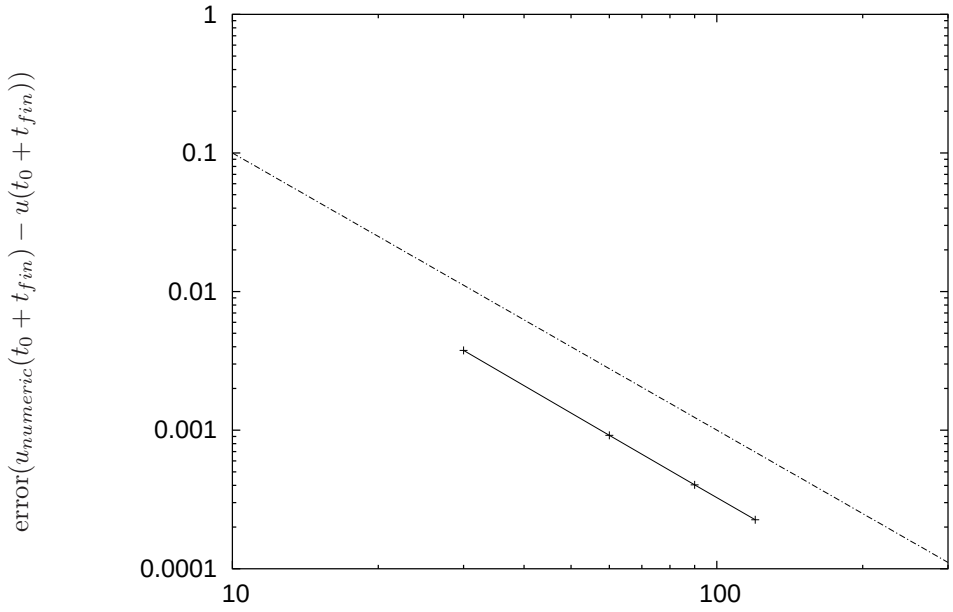

Figure 4.1: Maximum relative error of velocity as a function of the number of (pressure) grid nodes when solving the Taylor-Green problem without embedded boundaries. The chain-dotted straight reference line is proportional to N^{-2}.

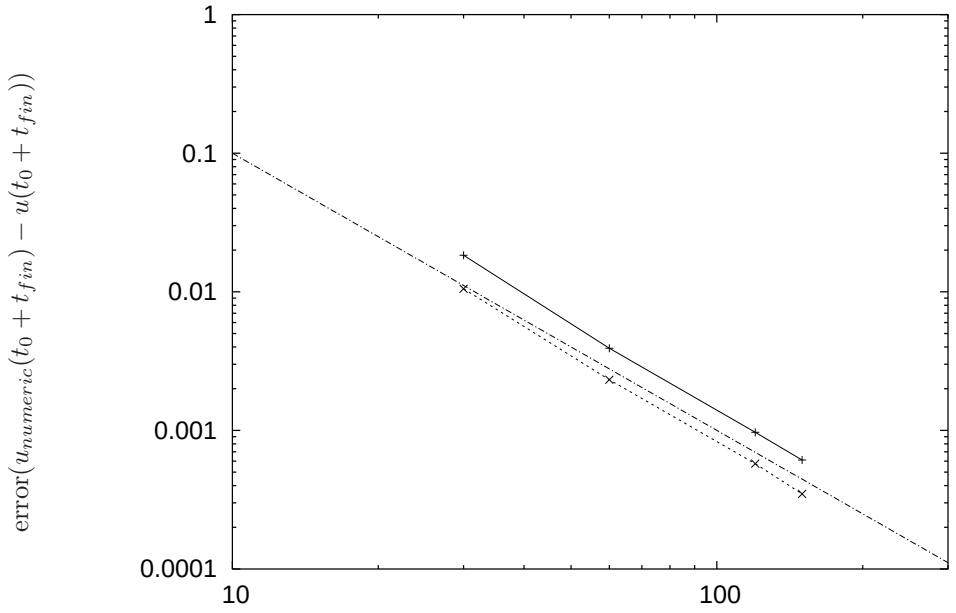

Figure 4.2: Maximum relative error of velocity as a function of the number of (pressure) grid nodes when solving the Taylor-Green problem in a circular sub-domain, using the present forcing method and the four-point regularized delta function of reference [7] (———), the three-point variant of reference [8] (– – – –). The chain-dotted straight reference line is proportional to N^{-2}.

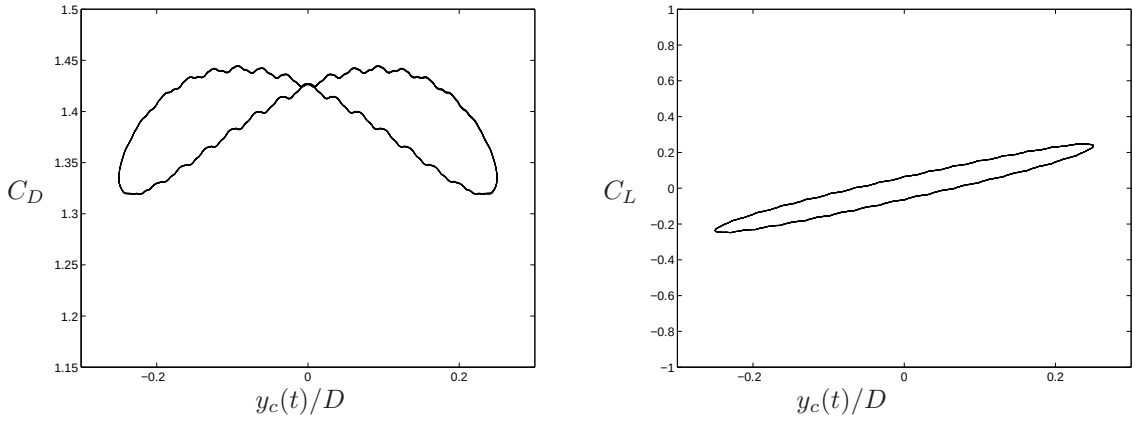

Figure 4.3: Dimensionless coefficients obtained by the present method in the case of a translationally oscillating cylinder in uniform cross-flow at $Re_D = 185$, a grid dimension of 1024×1024 and a time step of $\Delta t = 0.003$. The plots show phase-space diagrams of drag coefficient versus cylinder position (left) and lift coefficient vs. cylinder position (right). The arrows indicate the direction of the trajectories in time.

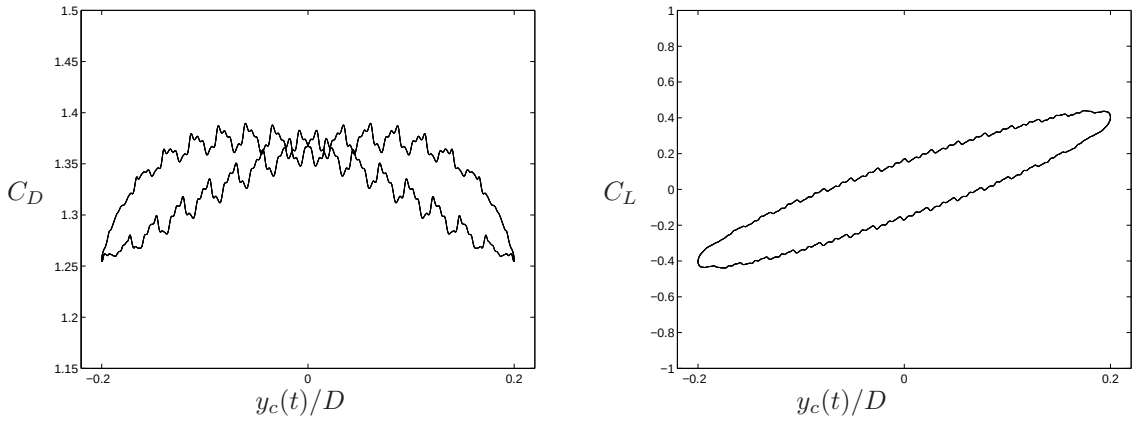

Figure 4.4: As figure 4.3, but using the IB method with the parameters $\kappa 10^5$, $\gamma = 10$ and the reduced time-step of $\Delta t = 0.0005$.

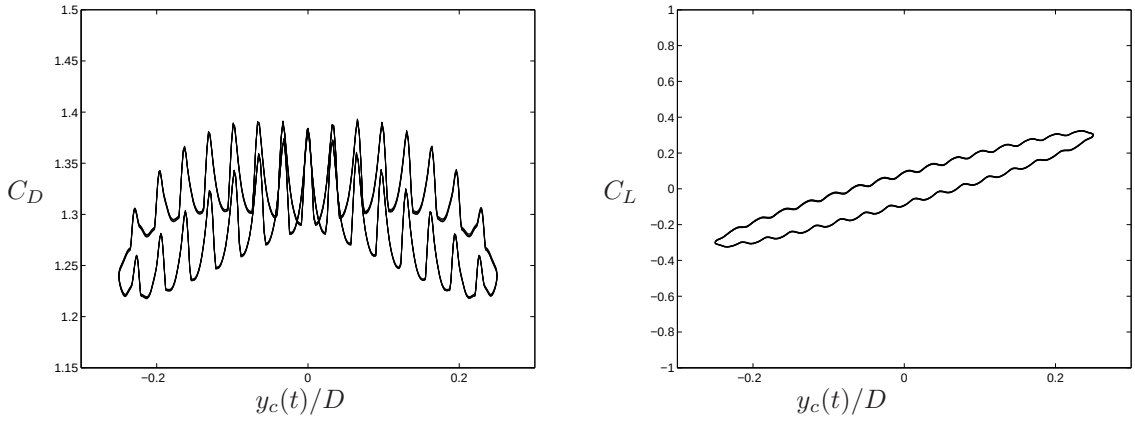

Figure 4.5: As figure 4.3, but using the method of reference [6], implemented in a divergence-free manner as shown in [1].

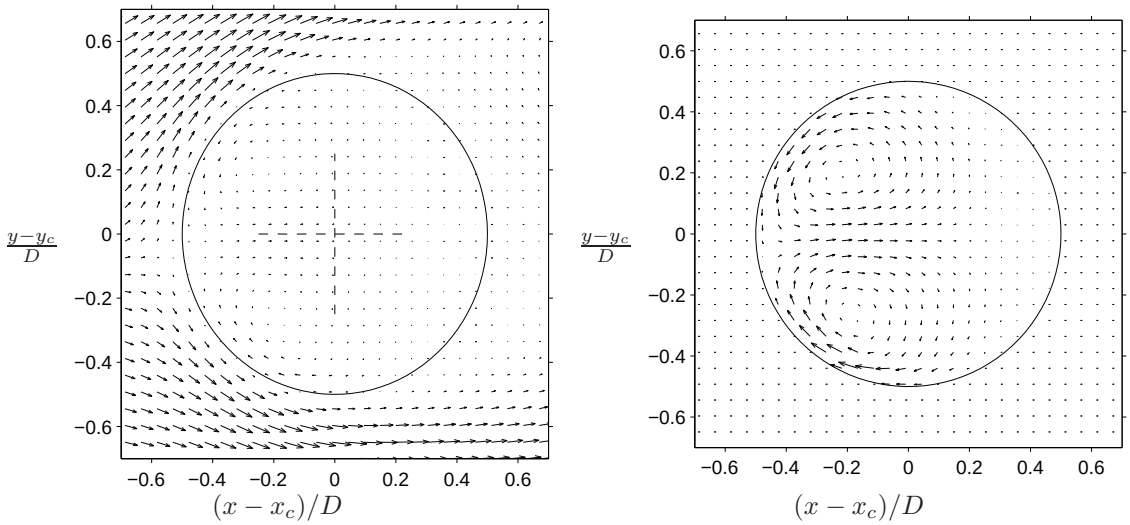

Figure 4.6: Vector plot of the velocity field in the vicinity of the oscillating cylinder. The field in a frame of reference moving with the cylinder (left); the deviation from exact rigid-body motion inside the cylinder (right). Note that the scale of the arrows is different between the two plots. The current phase angle is 2.6138 (in radians) and the maximum deviation is $0.279u_\infty$.

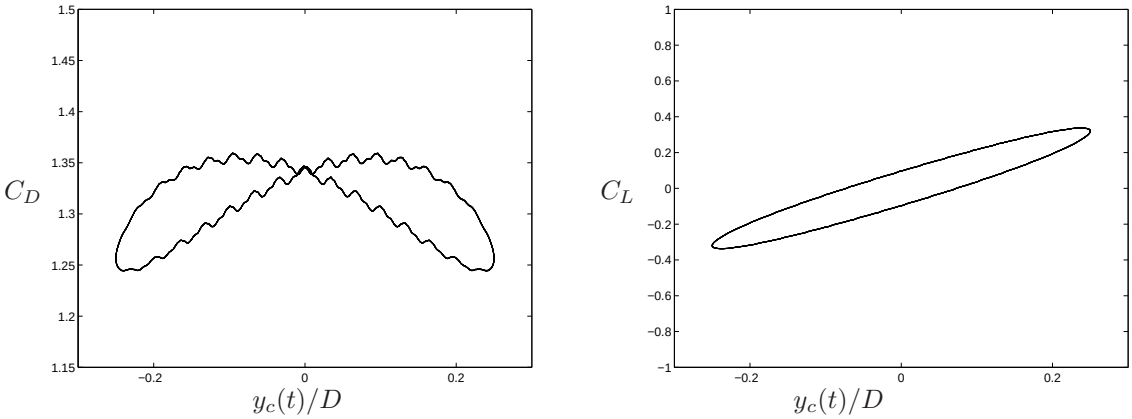

Figure 4.7: As figure 4.3, but forcing is applied throughout the solid domain.

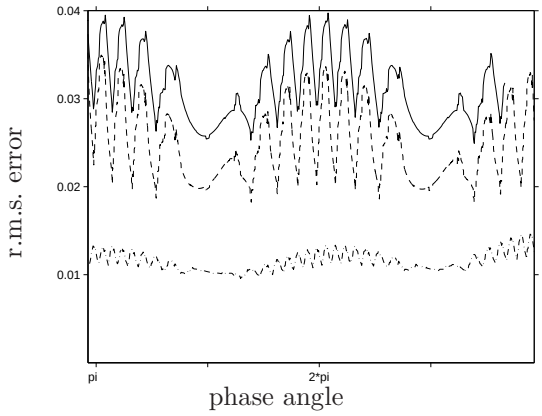

Figure 4.8: The deviation from rigid-body motion inside the oscillating cylinder of § 3.3 computed by the present method and forcing the entire solid domain. —— 512×512, $\Delta t = 0.003$; - - - - 512×512, $\Delta t = 0.0003$; —·— 1024×1024, $\Delta t = 0.003$. Please note that the abscissa does not start with zero phase angle.

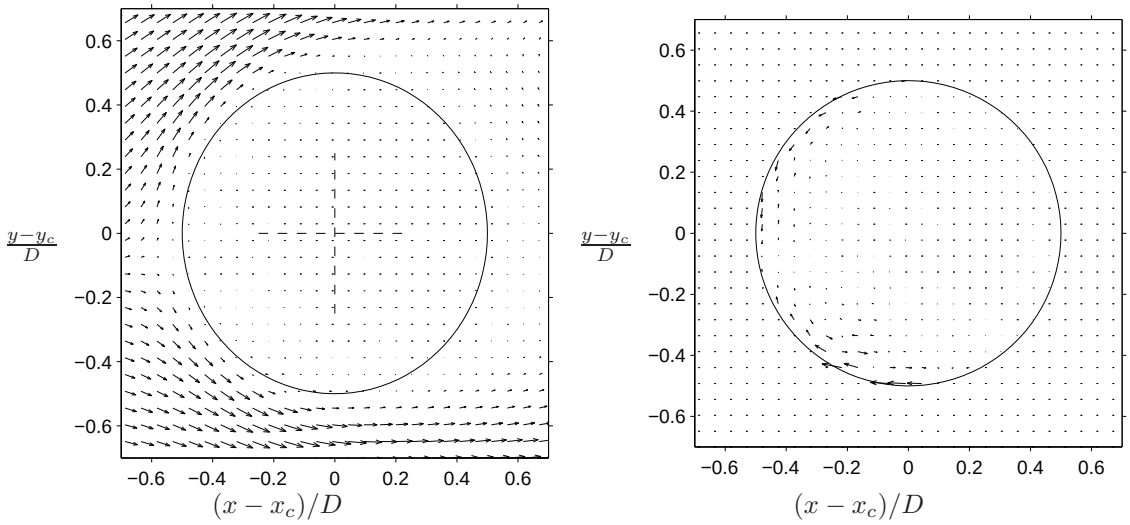

Figure 4.9: As figure 4.6, but forcing the entire solid domain. The maximum deviation is $0.137u_\infty$.

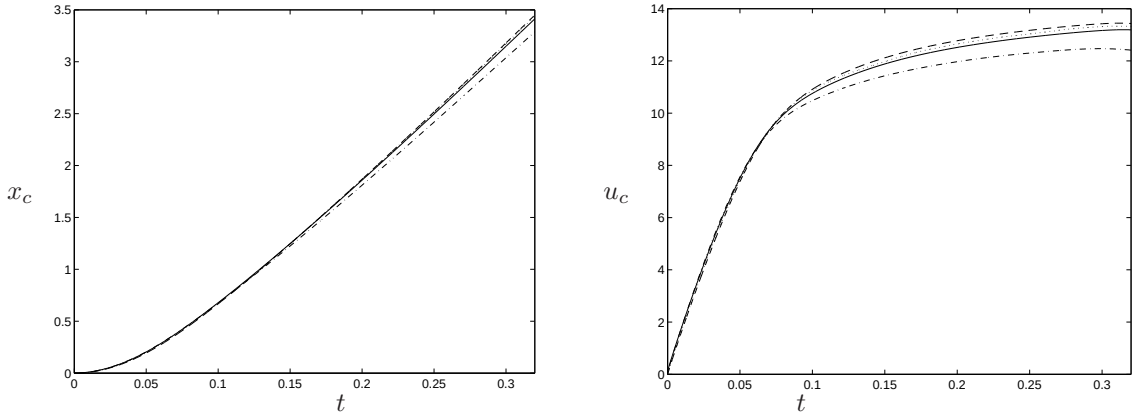

Figure 4.10: A single particle with density $\rho_p/\rho_f = 1.5$ and radius $r_c = 0.125$, freely accelerating from rest under the acton of gravity $|\mathbf{g}| = 981$ in an initially ambient fluid with viscosity $\nu = 0.01$. ——— results obtained with the present method; – – – – results obtained with the present method, but also forcing the inside of the solid domain; ····· results from the immersed boundary method ($\kappa = 10^7$, $\gamma = 100$); —·— results provided by T.-W. Pan, University of Houston.

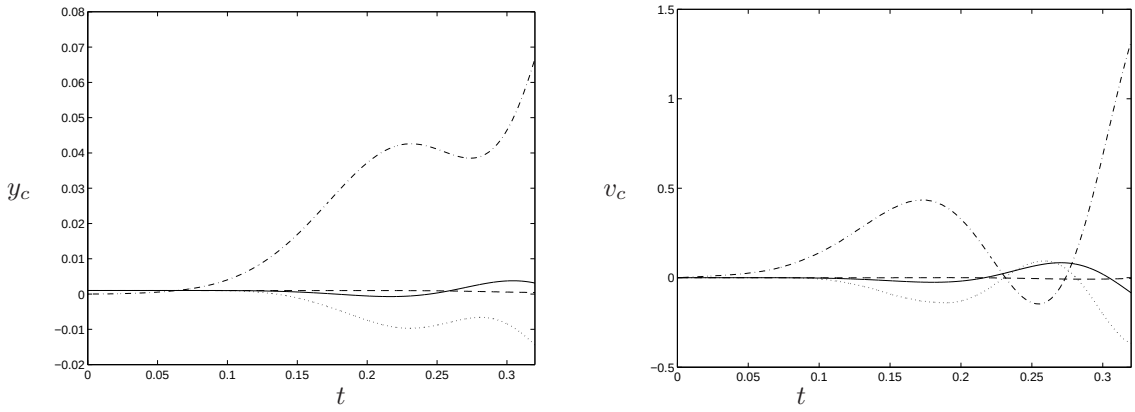

Figure 4.11: As figure 4.11, but showing horizontal position and velocity. ——— results obtained with the present method; – – – – results obtained with the present method, but also forcing the inside of the solid domain; ····· results from the immersed boundary method ($\kappa = 10^7$, $\gamma = 100$); —·— results provided by T.-W. Pan, University of Houston.

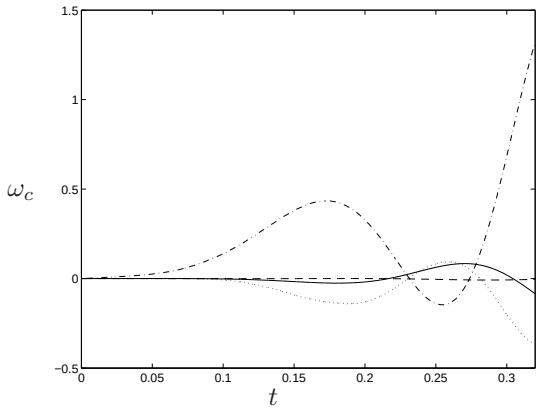

Figure 4.12: As figure 4.11, but showing angular velocity. ——— results obtained with the present method; - - - - results obtained with the present method, but also forcing the inside of the solid domain; ····· results from the immersed boundary method ($\kappa = 10^7$, $\gamma = 100$); —·— results provided by T.-W. Pan, University of Houston.

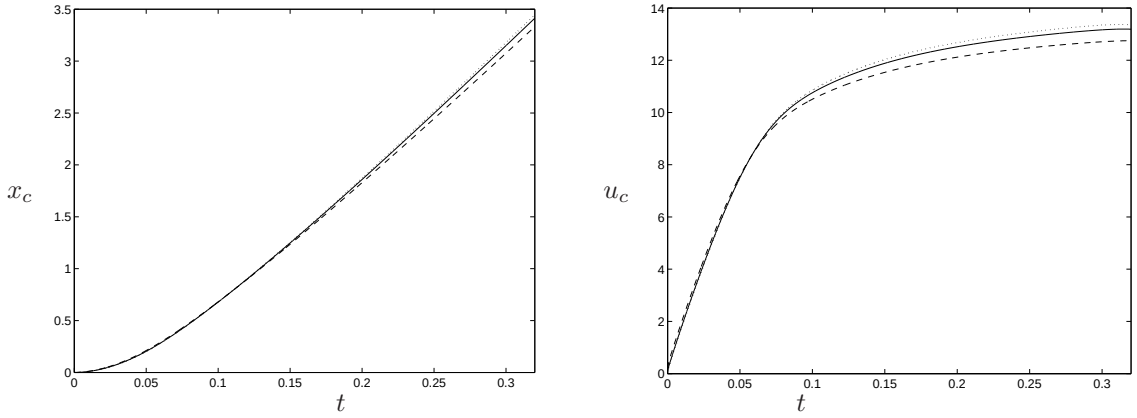

Figure 4.13: Case of figure 4.10. Comparison of results from the present method (ring forcing) for different time steps: - - - - $\Delta t = 0.00025$; ——— $\Delta t = 0.0001$; ····· $\Delta t = 0.00005$.

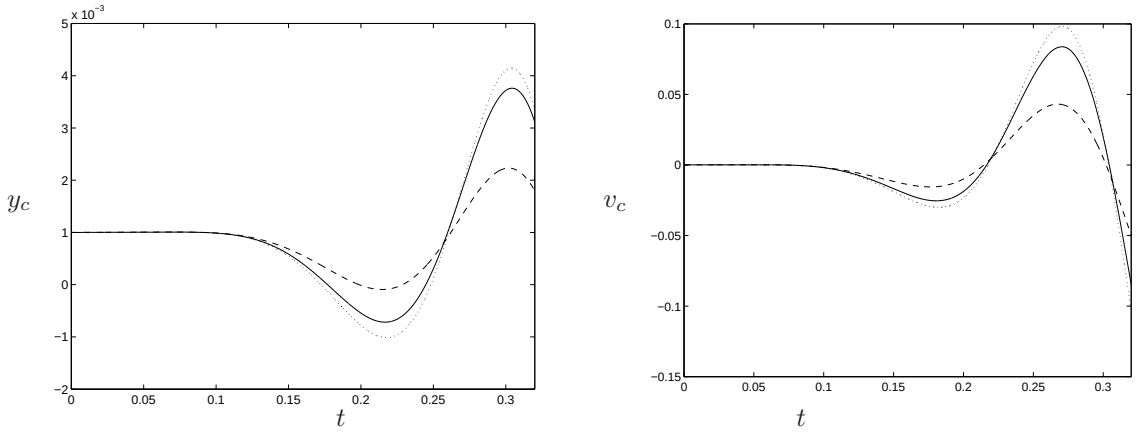

Figure 4.14: Case of figure 4.10. Comparison of results from the present method (ring forcing) for different time steps: - - - - $\Delta t = 0.00025$; ——— $\Delta t = 0.0001$; ····· $\Delta t = 0.00005$.

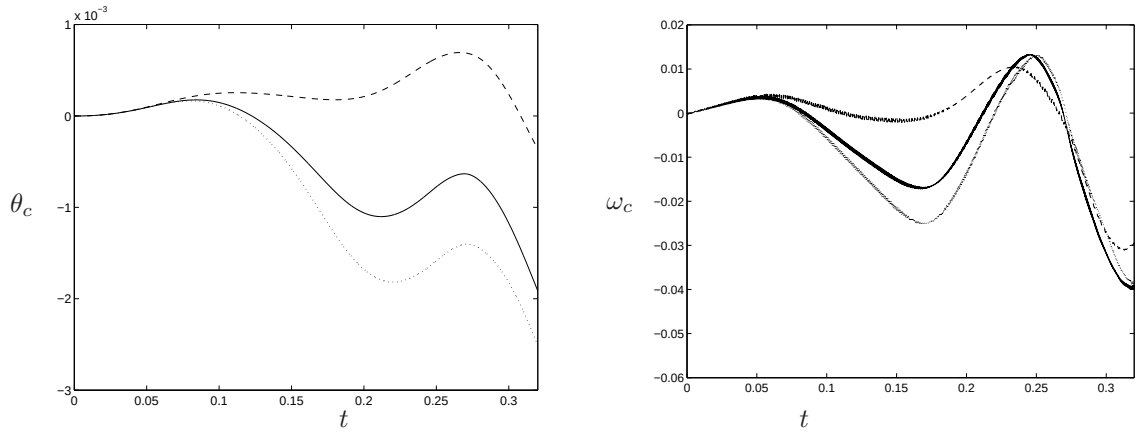

Figure 4.15: Case of figure 4.10. Comparison of results from the present method (ring forcing) for different time steps: - - - - $\Delta t = 0.00025$; ——— $\Delta t = 0.0001$; ····· $\Delta t = 0.00005$.

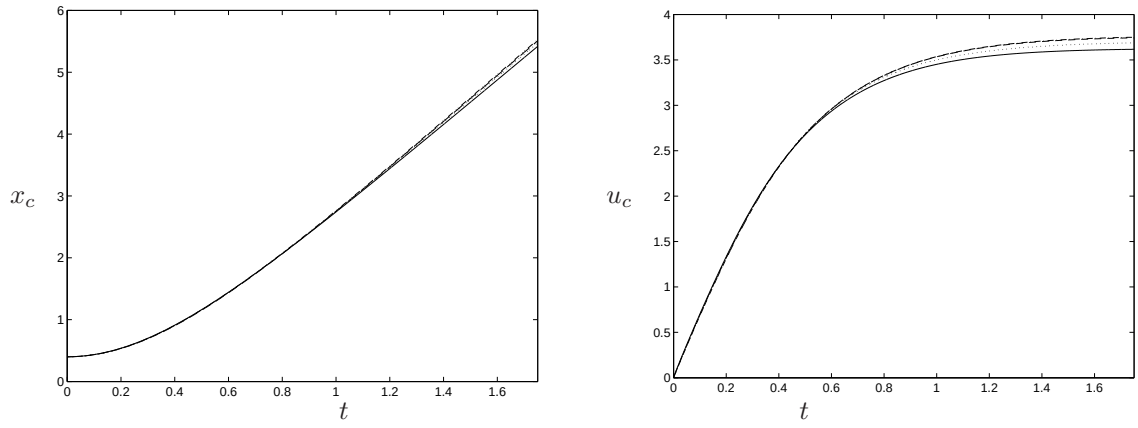

Figure 4.16: A single particle with density $\rho_p/\rho_f = 8$ and radius $r_c = 0.1$, freely accelerating from rest under the acton of gravity $|\mathbf{g}| = 9.81$ in an initially ambient fluid with viscosity $\nu = 0.005$. ——— results obtained with the present method; - - - - results obtained with the present method, but also forcing the inside of the solid domain; ····· results from the immersed boundary method ($\Delta t = 0.0002$, $\kappa = 2 \cdot 10^5$, $\gamma = 50$); —·— results from the method of [6]

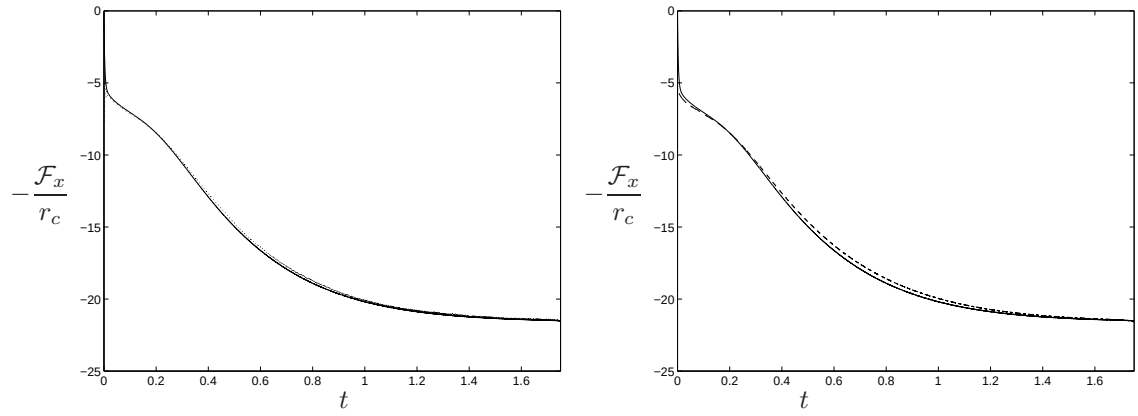

Figure 4.17: Sedimentation of a single particle with $\rho_p/\rho_f = 8$. Comparison of the vertical hydrodynamical force over time: present vs. immersed boundary method ($\Delta t = 0.0002$, $\kappa = 2 \cdot 10^5$, $\gamma = 50$; left); present vs. present method with forcing in the entire solid domain (right).

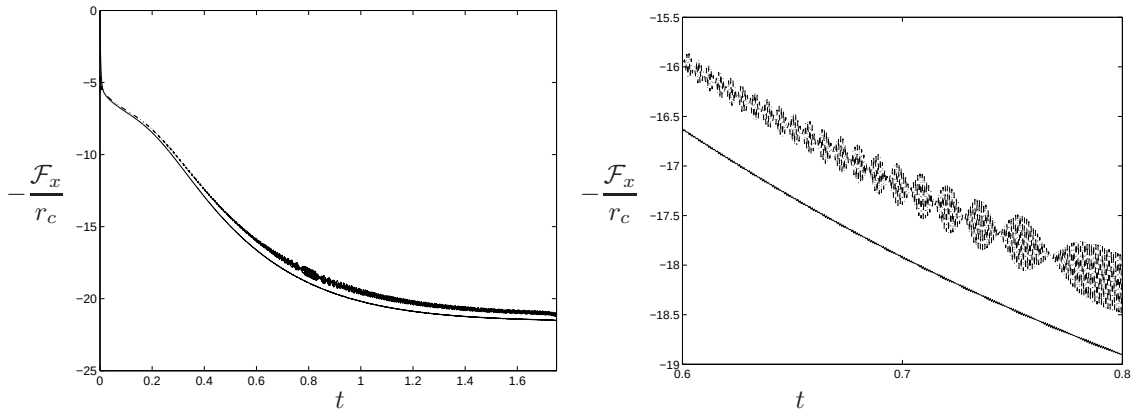

Figure 4.18: Sedimentation of a single particle with $\rho_p/\rho_f = 8$. Comparison of the vertical hydrodynamical force over time: present method vs. method of [6]. The plot on the right shows a zoom of the same data.

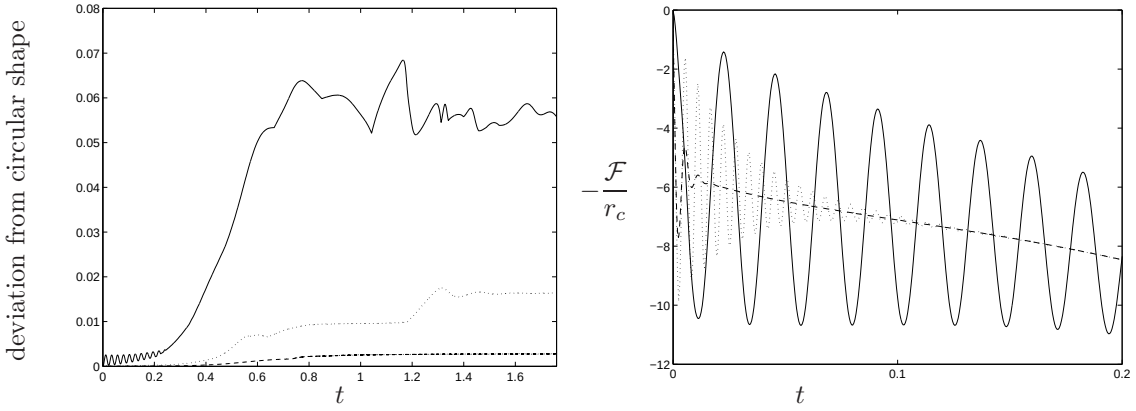

Figure 4.19: Case of a single particle sedimenting (cf. figure 4.16) . Results obtained by the immersed boundary method: maximum deviation from circular shape, normalized by the particle radius (left); vertical hydrodynamical force during the start-up process (right). The line styles correspond to: —— $\kappa = 1.25 \cdot 10^4$, $\gamma = 0$, $\Delta t = 0.0005$; ····· $\kappa = 2 \cdot 10^5$, $\gamma = 5$, $\Delta t = 0.0005$; —·— $\kappa = 1 \cdot 10^6$, $\gamma = 5$, $\Delta t = 0.0002$; - - - - $\kappa = 2 \cdot 10^5$, $\gamma = 50$, $\Delta t = 0.0002$.

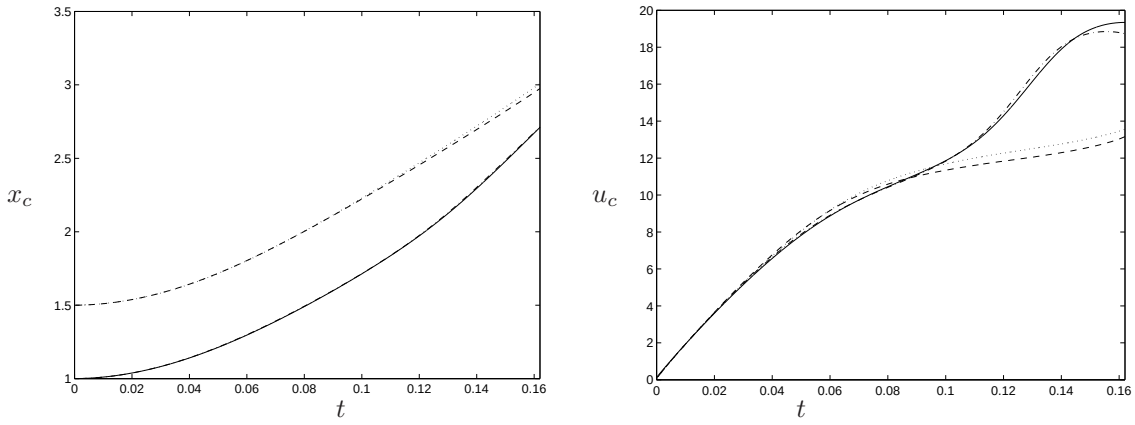

Figure 4.20: Wake interaction of two sedimenting particles with density $\rho_p/\rho_f = 1.5$ which are initially aligned vertically. Results obtained with the present method, $\Delta t = 0.0001$, $\Delta x = 1/256$: ——— trailing, ····· leading. Results provided by T.-W. Pan, University of Houston: —·— trailing, – – – – leading. Vertical position (left), vertical velocity (right).

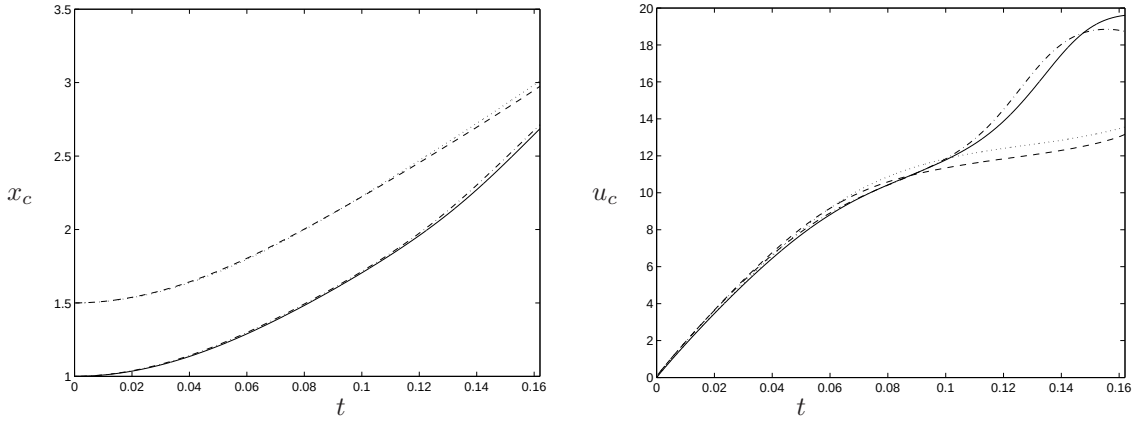

Figure 4.21: Wake interaction of two sedimenting particles with density $\rho_p/\rho_f = 1.5$ which are initially aligned vertically. Results obtained with the IB method, $\kappa = 10^7$, $\gamma = 100$, $\Delta t = 0.0001$, $\Delta x = 1/256$: ——— trailing, ····· leading. Results provided by T.-W. Pan, University of Houston: —·— trailing, – – – – leading. Vertical position (left), vertical velocity (right).

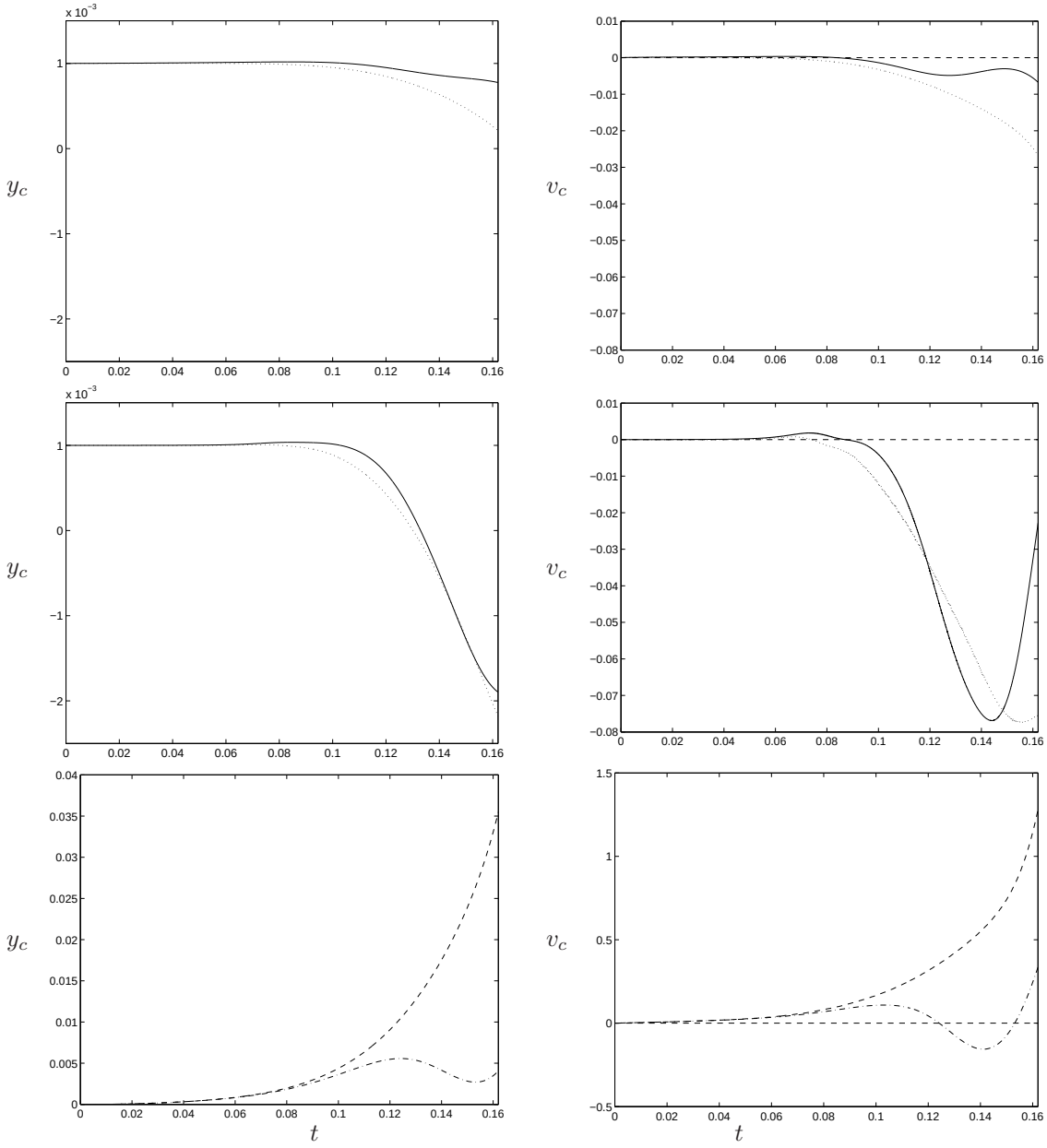

Figure 4.22: Horizontal position (left column) and horizontal velocity (right column) vs. time during the interaction of two sedimenting particles with density $\rho_p/\rho_f = 1.5$ which are initially aligned vertically. Top row: results obtained with the present method, ——— trailing, ····· leading. Center row: original IB method, ——— trailing, ····· leading. Bottom row: results provided by T.-W. Pan, University of Houston, —·— trailing, – – – leading. Please note the differences in scale.

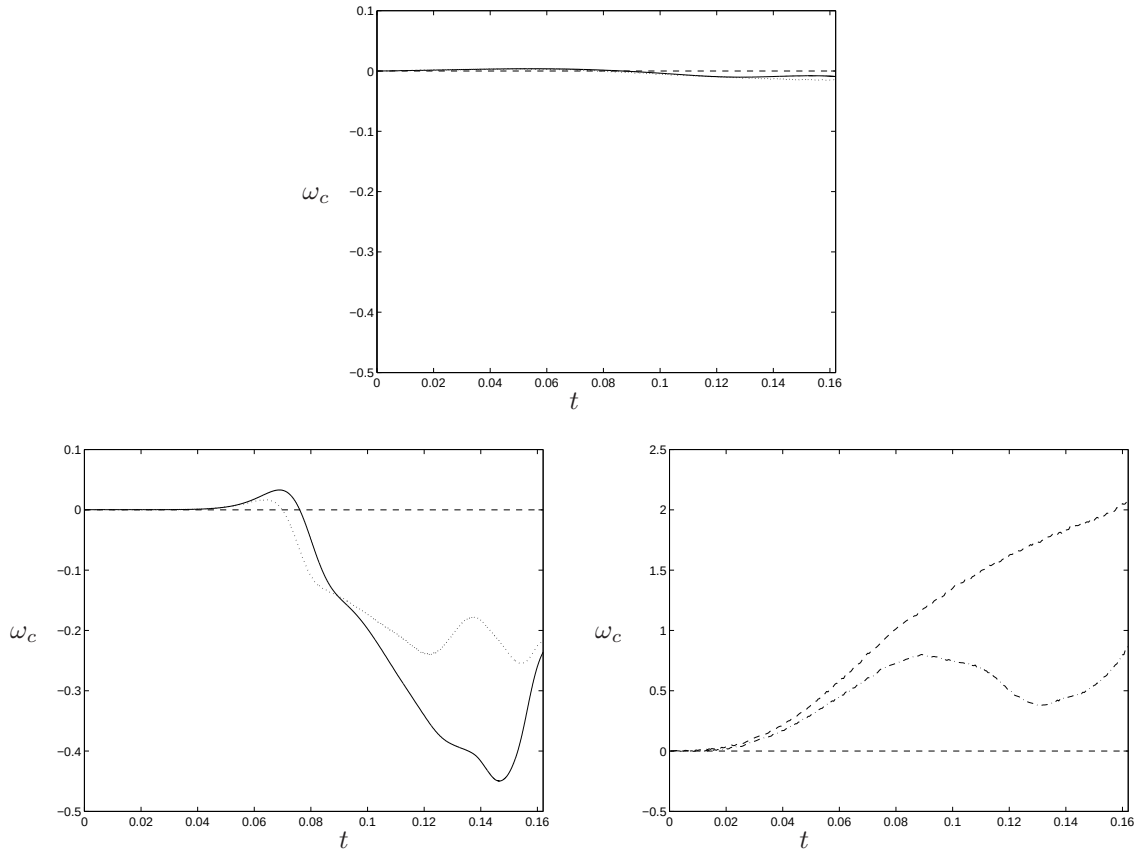

Figure 4.23: Rotational velocity vs. time during the interaction of two sedimenting particles with density $\rho_p/\rho_f = 1.5$ which are initially aligned vertically. Top graph: results obtained with the present method, ——— trailing, ····· leading. Bottom left: original IB method, ——— trailing, ····· leading. Bottom right: results provided by T.-W. Pan, University of Houston, —·— trailing, – – – – leading. Please note the differences in scale.

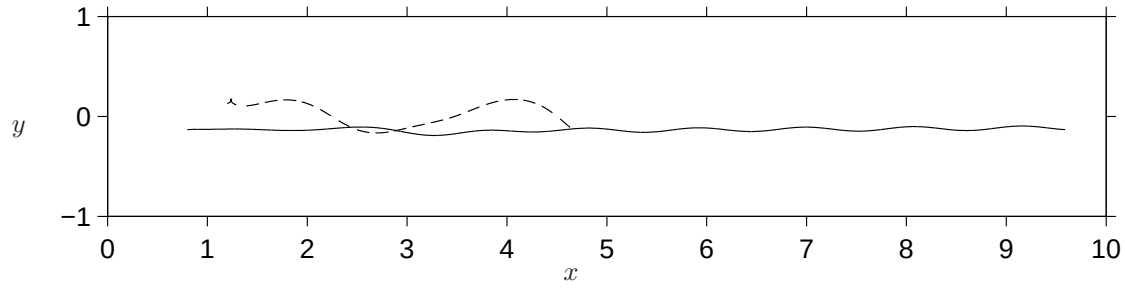

Figure 4.24: Wake interaction of two sedimenting particles with density $\rho_p^{(1)}/\rho_f = 1.4$, $\rho_p^{(1)}/\rho_f = 1.05$ and initial vertical and lateral offset. The gravity acts in the positive x-direction. Results obtained with the present method, $\Delta t = 0.0015$, $\Delta x = 1/200$. Trajectories of the heavy particle (———) and the light particle (– – – –).

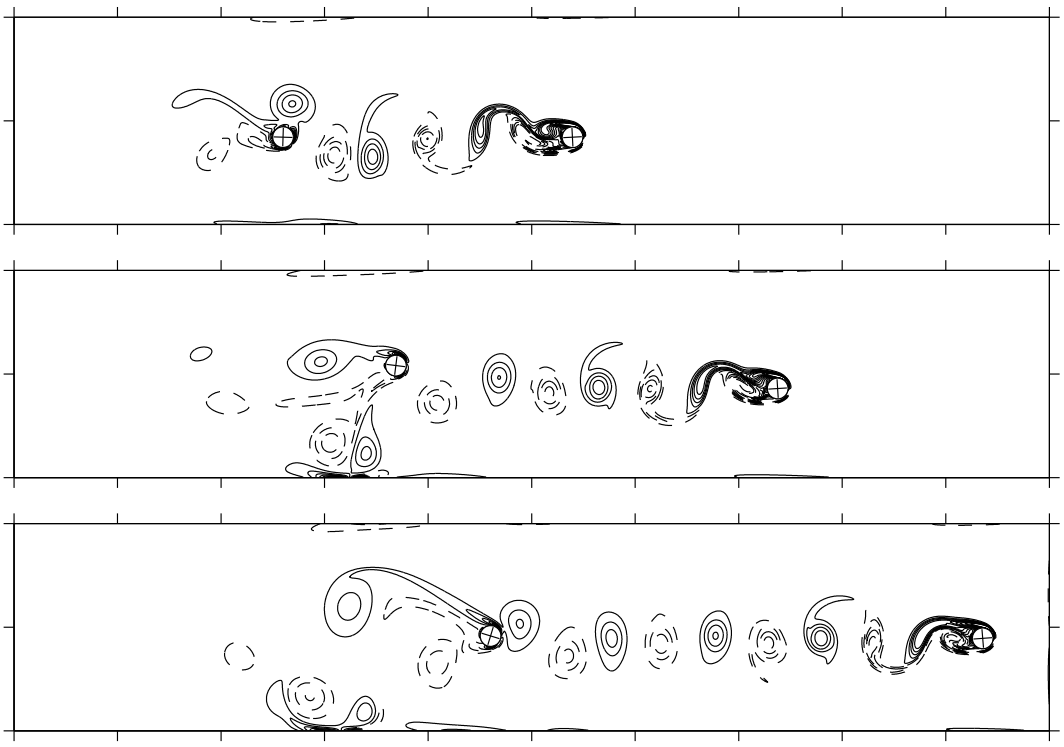

Figure 4.25: Wake interaction of two sedimenting particles with density $\rho_p^{(1)}/\rho_f = 1.4$, $\rho_p^{(1)}/\rho_f = 1.05$ and initial vertical and lateral offset. The gravity acts in the positive x-direction. Results obtained with the present method, $\Delta t = 0.0015$, $\Delta x = 1/200$. Instantaneous contours of vorticity (values at -30:3:30, negative values corresponding to dashed lines) and particle positions at times $t = 5.25$, $t = 7.35$, $t = 9.45$ (from top to bottom). The crosses inside the circles indicate the angular position of the particles.

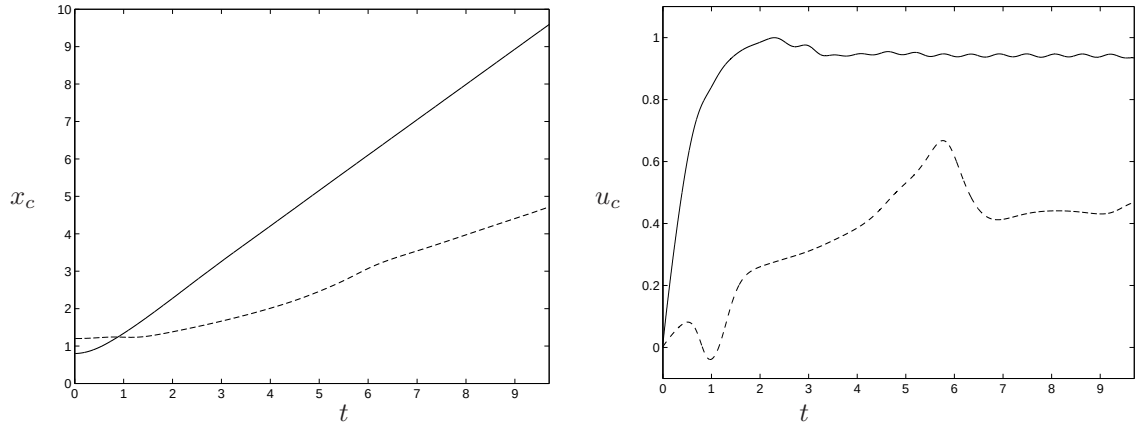

Figure 4.26: Wake interaction of two sedimenting particles with density $\rho_p^{(1)}/\rho_f = 1.4$, $\rho_p^{(1)}/\rho_f = 1.05$ and initial vertical and lateral offset. Results obtained with the present method, $\Delta t = 0.0015$, $\Delta x = 1/200$: —— heavy particle, - - - - light particle. Vertical position (left), vertical velocity (right).

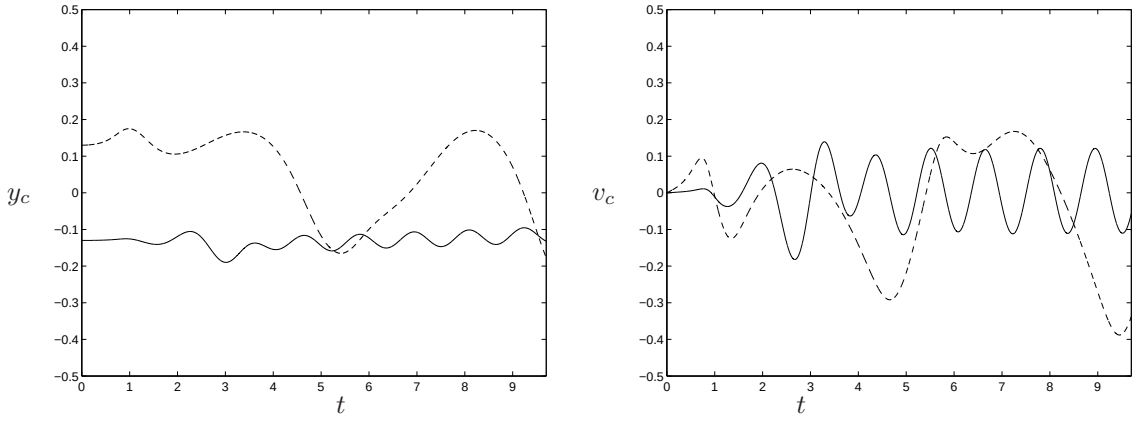

Figure 4.27: Wake interaction of two sedimenting particles with density $\rho_p^{(1)}/\rho_f = 1.4$, $\rho_p^{(1)}/\rho_f = 1.05$ and initial vertical and lateral offset. Results obtained with the present method, $\Delta t = 0.0015$, $\Delta x = 1/200$: —— heavy particle, - - - - light particle. Horizontal position (left), horizontal velocity (right).

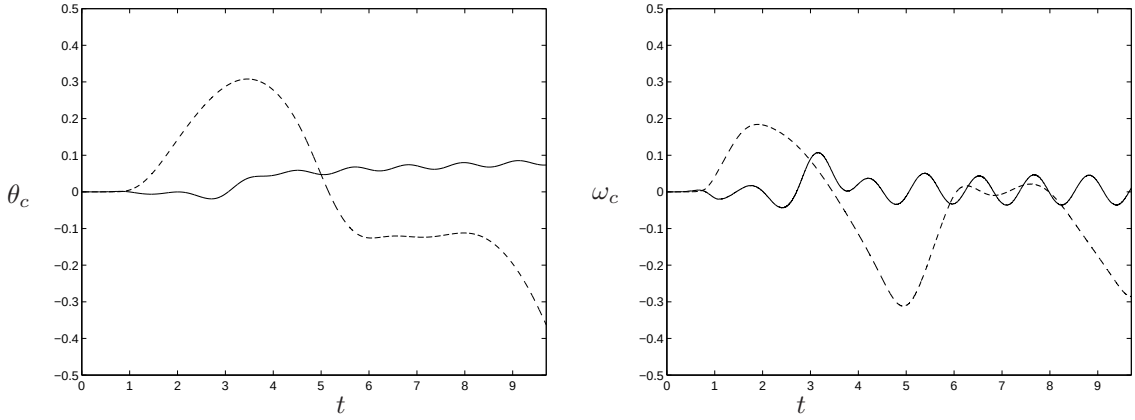

Figure 4.28: Wake interaction of two sedimenting particles with density $\rho_p^{(1)}/\rho_f = 1.4$, $\rho_p^{(1)}/\rho_f = 1.05$ and initial vertical and lateral offset. Results obtained with the present method, $\Delta t = 0.0015$, $\Delta x = 1/200$: —— heavy particle, - - - - light particle. Angular position in radians (left), angular velocity in radians per unit time (right).

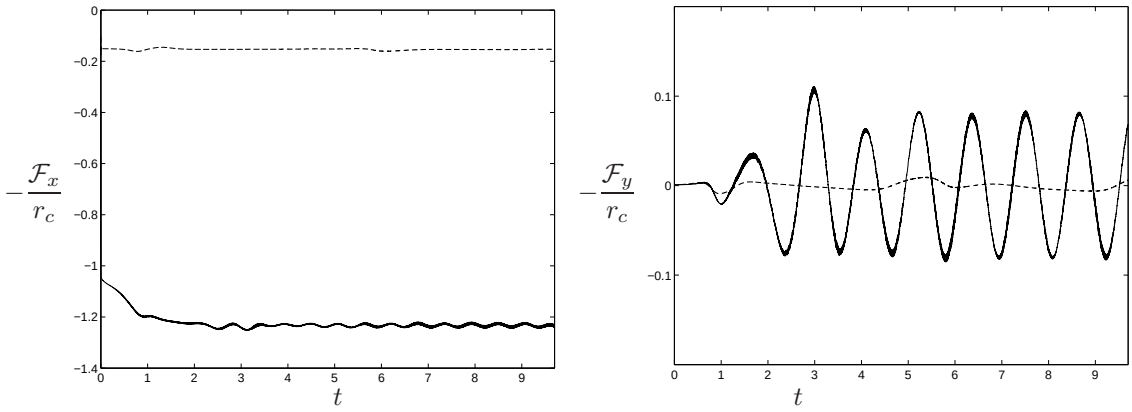

Figure 4.29: Wake interaction of two sedimenting particles with density $\rho_p^{(1)}/\rho_f = 1.4$, $\rho_p^{(1)}/\rho_f = 1.05$ and initial vertical and lateral offset. Results obtained with the present method, $\Delta t = 0.0015$, $\Delta x = 1/200$: ——— heavy particle, - - - - light particle. Vertical hydrodynamic force (left), horizontal hydrodynamic force (right).

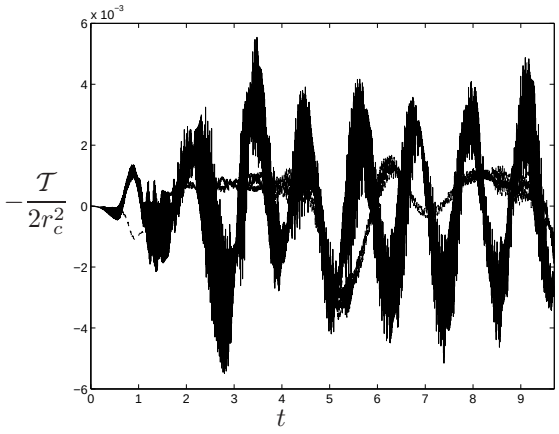

Figure 4.30: Wake interaction of two sedimenting particles with density $\rho_p^{(1)}/\rho_f = 1.4$, $\rho_p^{(1)}/\rho_f = 1.05$ and initial vertical and lateral offset. Results obtained with the present method, $\Delta t = 0.0015$, $\Delta x = 1/200$: ——— heavy particle, - - - - light particle. Torque acting on the particle.